Max-Planck-Institut für Meteorologie
Max Planck Institute for Meteorology

Aerosol Indirect Effect in the Thermal Spectral Range as Seen from Satellites

Abhay Devasthale

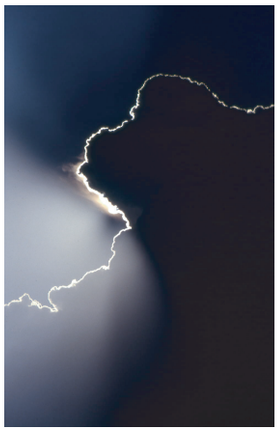

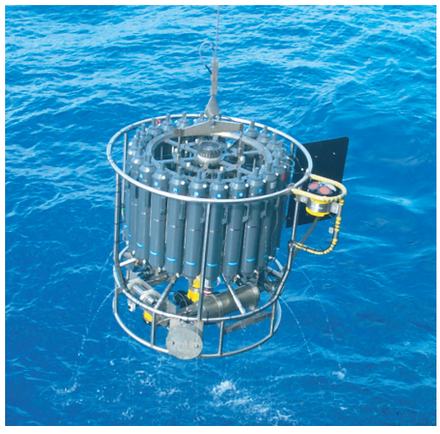

Berichte zur Erdsystemforschung 16/2005

Reports on Earth System Science

Hinweis

Die Berichte zur Erdsytemforschung werden vom Max-Planck-Institut für Meteorologie in Hamburg in unregelmäßiger Abfolge herausgegeben.

Sie enthalten wissenschaftliche und technische Beiträge, inklusive Dissertationen.

Die Beiträge geben nicht notwendigerweise die Auffassung des Instituts wieder.

Die "Berichte zur Erdsystemforschung" führen die vorherigen Reihen "Reports" und "Examensarbeiten" weiter.

Notice

The Reports on Earth System Science are published by the Max Planck Institute for Meteorology in Hamburg. They appear in irregular intervals.

They contain scientific and technical contributions, including Ph. D. theses.

The Reports do not necessarily reflect the opinion of the Institute.

The "Reports on Earth System Science" continue the former "Reports" and "Examensarbeiten" of the Max Planck Institute.

Anschrift / Address

Max-Planck-Institut für Meteorologie
Bundesstrasse 53
20146 Hamburg
Deutschland

Tel.: +49-(0)40-4 11 73-0
Fax: +49-(0)40-4 11 73-298
Web: www.mpimet.mpg.de

Layout:

Bettina Diallo, PR & Grafik

Titelfotos:
vorne:
Christian Klepp - Jochem Marotzke - Christian Klepp
hinten:
Katsumasa Tanaka - Christian Klepp - Clotilde Dubois

Berichte zur Erdsytemforschung 16/2005

Aerosol Indirect Effect in the Thermal Spectral Range as Seen from Satellites

Dissertation zur Erlangung des Doktorgrades der Naturwissenschaften
im Fachbereich Geowissenschaften der Universität Hamburg
vorgelegt von

Abhay Devasthale
aus Ahmednagar (M.S.), Indien

Hamburg 2005

Reports on Earth System Science 16/2005

ISSN 1614-1199

Abhay Devasthale
Max-Planck-Institut für Meteorologie
Bundesstrasse 53
20146 Hamburg
Germany

Als Dissertation angenommen
vom Fachbereich Geowissenschaften der Universität Hamburg

auf Grund der Gutachten von
Prof. Dr. Hartmut Graßl
und
Dr. Olaf Krüger

Hamburg, den 25. Oktober 2005
Professor Dr. Helmut Schleicher
Dekan des Fachbereiches Geowissenschaften

ISSN 1614-1199

Aerosol Indirect Effect in the Thermal Spectral Range as Seen from Satellites

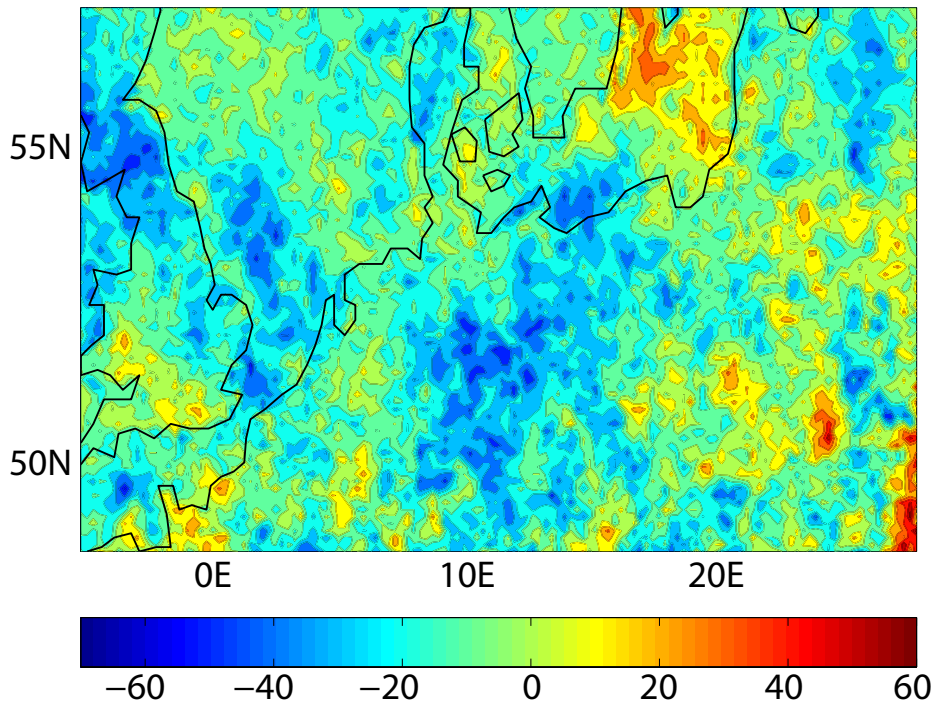

Changes in low, medium and convective cloud top temperatures (in Kx10) from the late 1980s to the late 1990s for summer season.

Abhay Devasthale

Hamburg 2005

Contents

Abstract

Insufficient knowledge about aerosol-cloud interactions has caused uncertainty in the Earth Radiation Budget. Lack of information about aerosol type, composition and concentration on global and regional scales also has restrained numerous efforts that have been made in the past to quantify the modulation of cloud properties by aerosols. Clouds, which cover more than half of the earth at any given time, have a key role in radiation budget. Most of the work has been done so far to understand modulation of cloud microphysical properties (in visible spectrum) by aerosols neglecting the thermal part. Satellites play unique role in improving knowledge about aerosol-cloud interactions through their ability to quantify spectral signatures of clouds and uniform, continuous sampling of the earth. Using long-term satellite data evaluations, this study reveals an entirely new aspect of these interactions and suggests that there exists indirect aerosol effect in the thermal spectrum. It suggests that anthropogenic aerosols, finer particles in particular, and cloud top temperature co-vary. This thermal effect could be equally important and hence cannot be neglected in radiation budget studies. First evidence of the impact of ship emissions on cloud properties over coastal waters is also presented.

Chapter 1

Introduction and motivation

1.1 Introduction

Aerosols of anthropogenic origin and their role in the climate of the Earth are being studied extensively in the last few decades. The questions like, *"Do aerosols through their complex interactions with clouds compensate the global warming? Or do they slow down the hydrological cycle? What exactly is their role in Earth's Radiation Budget (ERB)?"*, are being investigated and debated both on regional and global scales [1][2]. Still there remains high uncertainty in their role in the ERB and its magnitude [1]. This uncertainty arises, firstly, from the high spatio-temporal variability of aerosols. Secondly, their complex interactions with radiation and clouds are not fully understood and hence are not properly parameterised in regional or global numerical models. And thirdly, lack of observations on a global scale makes it further difficult to quantify direct and indirect effects of aerosols.

The ability of describing the spectral signatures of aerosols and clouds and their uniform sampling of the earth are making satellites increasingly useful in reducing this uncertainty. Several studies have been published on both regional and global scales to understand aerosol-cloud interactions with the help of remotely sensed data [3][4][5][6][7][8][9]. The findings presented in this dissertation will reveal an entirely new aspect of aerosol-cloud interactions.

The following sections explain the aerosol direct and indirect effects and the motivation for this study.

1.2 Aerosol-cloud interactions

Aerosols, the tiny particles suspended in the atmosphere, have manifold direct and indirect effects on the climate system. These effects are explained below with reference to Fig. 1.1. Aerosols enhance scattering or the absorption of solar radiation depending upon the type, composition and concentration. This is called the direct effect. An increase in the aerosol concentration leads to more cloud condensation nuclei reducing the cloud droplet radius and thus increasing cloud albedo. This is known as first indirect aerosol effect or Twomey effect. Numerous studies report observational evidence for this effect [5][6]. These smaller droplets are less efficient in coalescence resulting in longer cloud life time and reduced precipitation, the effect known as second indirect aerosol effect. There are only few studies that attempt to detect and quantify this effect [8].

Aerosols that are strongly absorbing, e.g. black carbon, can reduce cloud albedo. Solar heating of boundary layer by such aerosols can lead to surface warming, thus evaporating some of the clouds and allowing more solar radiation to reach the ground. This is termed semi-direct effect [2]. There is no observational evidence so far for this effect. The global mean top of the atmosphere aerosol forcing range from -0.5 to $+0.2 W/m^2$ as reported in different publications. The Intergovernmental Panel on Climate Change (IPCC) in its Third Assessment Report (2001) estimated the aerosol indirect forcing to be mainly negative reaching up to $2 W/m^2$ but with very low level of scientific understanding [1].

Inspite of having such a key role in the radiation budget and in earth's climate, quantification of the direct and indirect aerosol effect is rather difficult owing to limited knowledge about aerosol type, composition and concentration on a global scale.

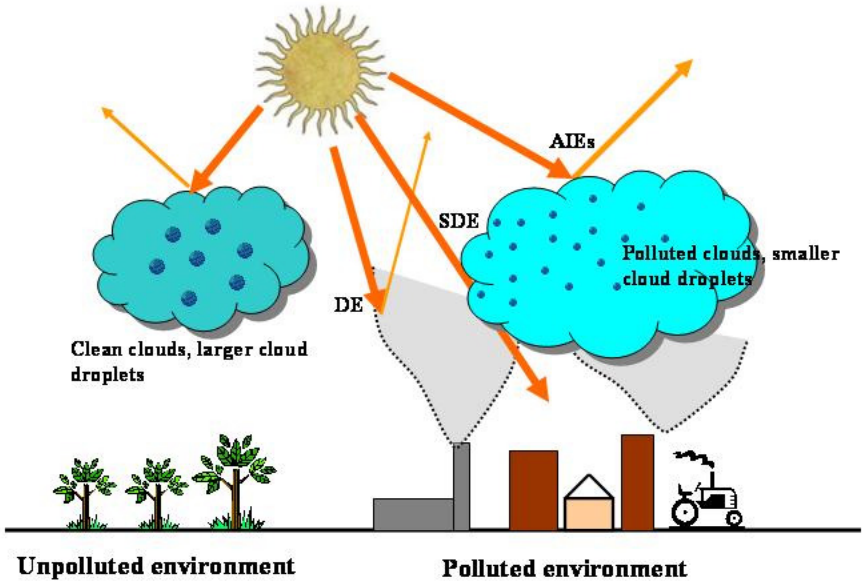

Figure 1.1: Direct and indirect aerosol effects. Clean clouds in unpolluted environment have larger droplets. Aerosols enhance scattering or absorption of solar radiation through the direct effect (DE). Polluted clouds have smaller droplets, increased cloud albedo, longer life time and reduced precipitation efficiency, combined in the indirect effects of aerosols (AIEs). Heating of the boundary layer can evaporate clouds allowing more solar radiation to reach the surface, termed semi-direct effect (SDE). Note: Figure not to the scale.

1.3 Background, hypothesis and outline of the thesis

As described above, emphasis so far has been to understand how aerosols modulate cloud albedo and microphysics. Observationally, this modulation results in a cloud reflectance change to be seen in the visible or near-infrared part of the electromagnetic spectrum. Cloud reflectance at visible and/or near-infrared wavelengths from satellite or airborne sensors are further used in many studies for the retrieval of microphysical properties of clean and polluted clouds, often in order to analyze indirect aerosol effects. But no study is known to me that examines an indirect aerosol effect in the thermal

part of the spectrum, which might be observed through a change in cloud top temperatures.

This study tries to present first evidence that there exists an indirect aerosol effect in the thermal range. Our hypothesis is that the increase in aerosol number concentration, in particular fine aerosols, may lift cloud tops thereby reducing cloud top temperatures and inducing higher variability. An increase in aerosol load lead to increase in cloud condensation nuclei and smaller cloud droplets. So the droplet growth by coalescence is less efficient. The updrafts in this case, out-balance the downdrafts and hence cloud tops are higher. Further, smaller droplets that are uplifted will freeze at higher altitudes releasing even more latent heat and resulting in increased convection. Two studies which are independent in their approach are explained here to detect increase in cloud tops due to the pollution.

Both studies are performed over Central or North-western Europe, mainly because more reliable emission inventories are available there compared to other regions of the world. The first study evaluates changes in cloud top temperatures over a part of Central Europe as a function of air pollution. Variability and changes in cloud top temperatures for the two distinct episodes of very high pollution (1985-88) and much lower pollution (1997-00) in terms of sulphur dioxide and particulate matter are analysed and compared using long-term satellite measurements from the same sensor type. Details are given in chapter 3.

Even though the pollution over land is decreasing, ship emissions over European seas continue to grow. From the year 2015 onwards, sulphur dioxide emissions from ships are projected to exceed those from land. 90 percent of all ship emissions originate from within 90 km of the coast. In that context, impact of these emissions on cloud properties over coastal areas is assessed in a second study. The study area is chosen in such a way that it covers the English Channel and the top three polluting harbours in Europe, namely Rotterdam (Netherlands), Antwerp (Belgium) and Milford Haven (United Kingdom). Details are given in chapter 4.

In all, almost ten years of satellite data from Advanced Very High Resolution Radiometer (AVHRR) onboard two NOAA satellites (NOAA-9 and NOAA-14) at 4 km spatial resolution are used. Also data from the Moderate Resolution Imaging Spectroradiometer (MODIS) onboard the Terra satellite and the Pathfinder AVHRR Land (PAL) dataset are used for validation. The total data size exceeds 800 Gigabytes. As the data are in raw format, a rigorous quality control is applied. All the technical details about data, its quality checks, calibration, cloud detection algorithm and validation are given in chapter 2. Chapter 5 concludes the thesis and an outlook is also presented.

Chapter 2

Radiometric calibration and validation

2.1 Satellite data and the AVHRR instrument

Satellites have become an integrate part of everyday human life since about 4 decades. Meteorological satellites, in particular, ever since the first launch in 1960, have contributed considerably to the understanding of the Earth system, which otherwise would not have been possible. Information regarding almost all components of the Earth system like atmosphere, land and biosphere and cryosphere has been extensively used by scientists in trying to understand processes, to monitor and manage earth resources and in planning. For example, our knowledge about clouds which are a very important but most uncertain component of the atmosphere has increased considerably because of the ability to detect cloud types, properties from the uniform and continuous observation of the entire globe from satellites in different spectral channels. To derive accurate and reliable information from the data, one has to understand the characteristics of the data, its preprocessing and finally, the retrieval algorithms for the desired products. This chapter provides technical details about the preprocessing steps of calibration, atmospheric correction

and validation of satellite data which are key steps in any remote sensing product generation scheme. The Global Area Coverage (GAC) data at nominal resolution of 4 km from AVHRR/2 onboard NOAA-9 and/or NOAA-14 are used in both studies. This GAC data in *level 1b* come in raw format, in the sense that data are encoded bitwise, not calibrated and not corrected for the atmospheric influence. Firstly, data are decoded, quality checks are applied to this raw data. This quality controlled data are then calibrated, atmospheric correction is applied, and finally the cloud detection algorithm separates clouds. Here only cloudy pixels are used for the statistical analysis.

AVHRR Instrument:
The AVHRR instrument has dimensions of $25cm \times 36cm \times 76cm$, weighs 27 kg and needs power of about 25 W. The instrument consists of a baseplate, a radiant cooler, the scanner assembly and an electronics unit. The base plate is a bench to which everything is attached. It has a blackbody acting as Internal Calibration Target (ICT) and four Platinum Resistance Thermometers (PRT) which measure the temperature of ICT. The scanner motor rotates at 360 rpm. The scan mirror makes an angle of 45° with the telescope axis and scans continuously in east-west direction with scanning angle of ± 55°. The optical subsystem consists of a 20 cm diameter afocal telescope and sets of dichroics, filters and detectors. The detectors for three thermal infrared channels are operated at $107K$. Five channel AVHRR/2 instrument has 2 channels in the solar spectrum, 2 channels in the thermal infrared window and one channel that is influenced by both the solar and thermal spectrum. Details are given below in Table 2.1.

2.2 Radiometric calibration

Radiometric calibration relates the output from the instrument to the intensity of the radiation incident on the instrument. In other words, the process to convert the detector output (which ranges from 0 to 1023, in case of

Table 2.1: Spectral bandwidth of AVHRR/2 channels

Channel	Spectral Range (μm)
1	0.58-0.68
2	0.725-1.10
3	3.55-3.93
4	10.30-11.30
5	11.50-12.50

AVHRR because of 10-bit radiometric resolution) into the reflectance/albedo or brightness temperature values. Various aspects of calibration include :

- Determination of spectral response function for all the channels
- Pre-launch calibration of all the channels
- In-flight calibration of thermal infrared channels
- Post-launch calibration

2.2.1 Spectral response function and pre-launch calibration

Detector is supposed to sense the radiation with wavelength λ within certain wavelength range λ_1 and λ_2. So the radiation received at the sensor is passed through the filter which should be opaque for $\lambda < \lambda_1$ and $\lambda > \lambda_2$ and should allow radiation within the λ_1 to λ_2 range. But the ideal filter does not exist. A full set of graphs of the spectral response functions are given in the NOAA Polar Orbiter Data Users Guide [11]. The values of the spectral response function for thermal channels are needed for in-flight radiometric calibration.

Pre-launch calibration is well described in [12]. In case of visible channels, the basic objective of pre-launch calibration is to establish simple regression between the reflectance factor of the integrating sphere source with that of

AVHRR digital counts under different illuminating conditions. An integrating sphere of 30 or 40 inches diameter with 12 lamps is used to compute the radiance values and detector output at different illuminating conditions. For the thermal channels, the tests are carried out in a vacuum test chamber which simulates space conditions. The scan mirror rotates at six revolutions per second. The output from each detector is amplified, digitised and recorded. The data are collected by changing the temperature of the laboratory blackbody between $175K$ and $315K$, in $10K$ steps between $175K$ and $290K$, in $5K$ steps above $290K$. This procedure is repeated for the three values of ICT temperatures of 10°C, 15°C and 20°C. AVHRR channels 3, 4 and 5 are calibrated by a two-point in-flight calibration using two sources of radiation, deep space and ICT. Thus for two points we have the values for temperature and digitised scanner output. Then straight line can be fitted to compute the relationship [10].

2.2.2 Post-launch calibration

Details of post-launch calibration are given below.

For solar channels:

There are three broad categories of methods available for the post-launch calibration of solar channels of satellite radiometers with no on-board calibration.

- Methods that use the simultaneous aircraft and satellite observations of a test area
- Methods that use both model simulations and satellite measurements
- Methods that apply statistical procedures to data to detect trends in the relative degradation of the radiometer.

So far, various methods of post-launch calibration have been developed using approaches mentioned above making it difficult to decide which one is better and more accurate. We assessed the impact of three well-known

calibration methodologies on cloud albedo. First one was proposed in [13]. It uses the south-eastern part of the Lybian desert as a radiometrically stable target and monitors the degradation of the AVHRR sensor. It is hereafter referred as RC method (Rao and Chen method). The second method [14] referred hereafter as KH method (Kaufman and Holben method) uses atmospheric scattering, ocean glint and desert reflection to calibrate AVHRR solar reflectances. And finally, the third method [15] referred to as CP method (Che and Price method) is just the linear regression of all the calibration coefficients derived from different methods. The variation in low level cloud albedo over the study area of Europe is shown in Fig. 2.1. All three methods result in different cloud albedos for the same month. Fortunately all methods show similar variability. So any method would be suitable for trend analysis. Also albedo values from all three methods show similar spatial pattern. For example, cloud albedo averaged for the month of May 1982 from these methods (Fig. 2.2) show similar spatial pattern. Further analysis and a simple comparison with the field experiment data from the MODIS Airborne Simulator (ASTEX, 1992, and WINTEX, 1999 Campaigns) show that albedos computed with the RC method are closer to reality and thus are used in this study.

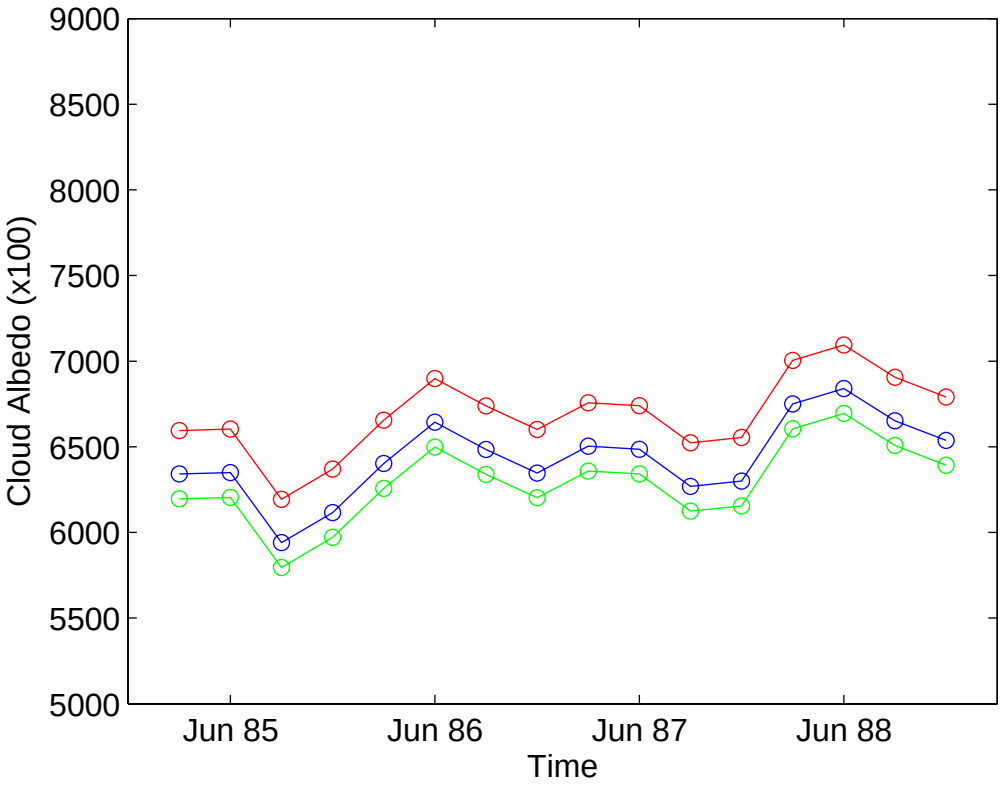

Figure 2.1: Variation of monthly mean low level cloud albedo for study area over Europe using three calibration methods (RC method: green, KH method: blue, and CP method: red) for the summer season (May, June, July and August) from 1985 to 1988.

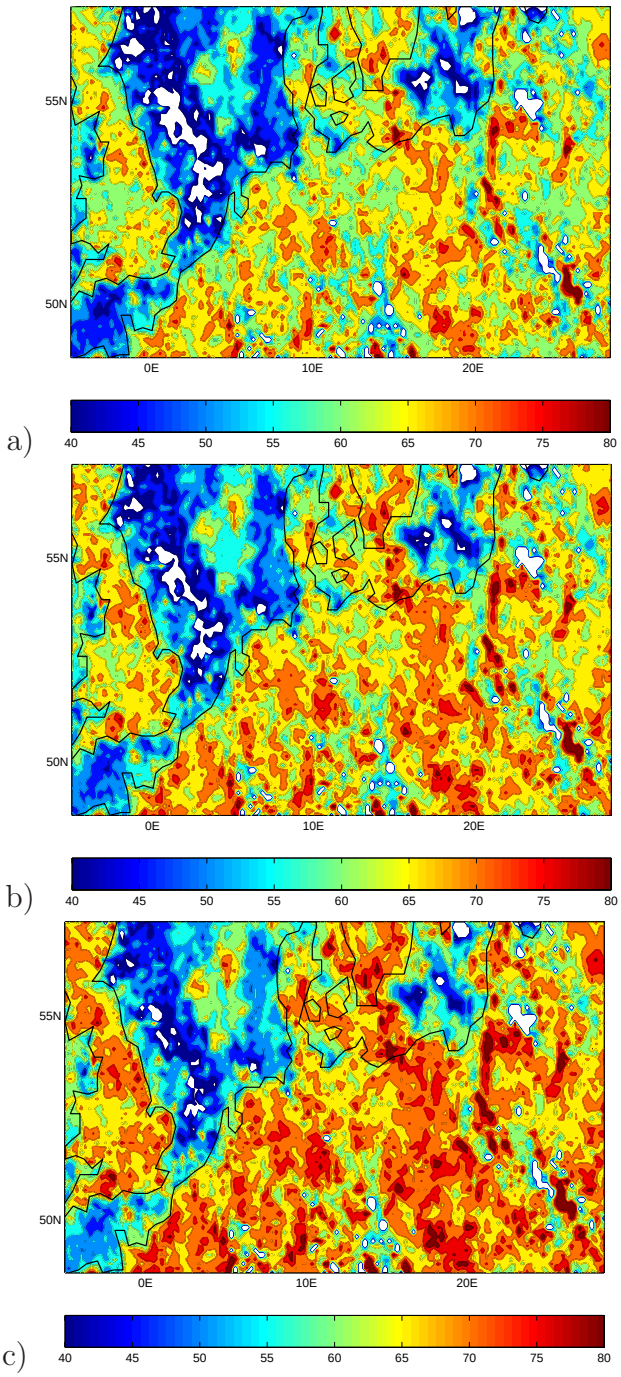

Figure 2.2: Cloud albedo averaged for the month of May 1982 from 3 different methods of calibration a) RC method, b) KH method, and c) CP method. While the methods show variation in albedo values, a similar spatial pattern is observed.

For thermal channels:

The radiance measured by the sensor (channel i) is computed as a linear function of the input data values as follows,

$$E_{lin} = S_i C + I_i \tag{2.1}$$

where E_{lin} is the radiance value in $W/(m^2 * sr * cm^{-1})$, C is the input data value (ranging from 0 to 1023 counts), and S_i and I_i are respectively the scaled slope and intercept values. The scaled thermal channel slope values are in units of $W/(m^2 * sr * cm^{-1})$ per count and the intercept is in $W/(m^2 * sr * cm^{-1})$. The conversion to brightness temperature from radiance is performed using the inverse of Planck's radiation equation as,

$$T(E) = \frac{C_2 \nu}{ln\left(1 + \frac{C_1 \nu^3}{E_{lin}}\right)} \tag{2.2}$$

where T is the temperature (K) for the radiance value E_{lin}, ν is the central wave number of the channel (cm^{-1}), and C_1 and C_2 are constants ($C_1 = 1.1910659 \times 10^{-5} W/(m^2 * sr * cm^{-4})$ and $C_2 = 1.438833 cmK$).

Nonlinearity correction : Hg-Cd-Te detectors are used in channels 4 and 5 of AVHRR, which are slightly nonlinear in their response to incoming radiation. The process responsible for this is the *Auger recombination* which results in an increase in the rate of recombination of electron hole pairs as the number density of electrons and holes increases at higher values of incoming radiance. We used the alternate method supplied by NESDIS for handling the nonlinearity which can be applied to radiances instead of brightness temperatures. For each instrument and for each channel, three coefficients (A, B, and D) of a quadratic equation are supplied in Section 1.4 of Polar Orbiter Users Guide [11] for all spacecraft from NOAA-13 onwards. The following quadratic equation can be used to compute the corrected radiance, RAD from the "linear" radiance, R_{lin} as,

$$RAD = AR_{lin} + BR_{lin}^2 + D \tag{2.3}$$

This new treatment of non-linearity should be an improvement over the previous method, because 1) it is less sensitive to noise in the thermal/vacuum test data, 2) it gives the user a choice of correcting either the radiance or the brightness temperatures, and 3) it has been applied retrospectively in the NOAA/NASA Pathfinder program [11].

2.2.3 Need for post-launch calibration

There are four important issues that determine the need for post-launch calibration of AVHRR data and the assessment of the accuracy of thermal channel calibration.

a. Effect of sensor degradation: Sensitivity of the sensor degrades with time. Various studies have shown that the sensitivity of the sensor has decreased with time and has affected the long-term records of AVHRR-derived products in climate and global change studies. Here, we take into account this degradation and compute the correct calibration coefficients to avoid any trend obtained to be misinterpreted. Fig. 2.3 shows the rather strong degradation rates for the solar channels of NOAA-7, -9 and -11.

b. Effect of orbital drift: The NOAA satellites are designed to operate in a sun-synchronous orbit to provide daily observations at the same local time. But especially in the case of afternoon satellites providing daylight measurements there is normally a drift to later observation time. This affects the measured signal because of changing attenuation of incoming radiation and surface anisotropy under changing illumination conditions. The Fig. 2.4 shows how the local observation time for different satellites has changed with time.

c. Effect of solar contamination and inconsistency of PRT and ICT values: The response of ICT is assumed to be invariant in time. But there can be a change in the response of ICT because of sunlight impinging on the baseplate which causes disagreement between the sensor measured radiometric output of the onboard blackbody and its bulk temperature measured by the PRTs. This effect occurs as the spacecraft moves out of the shadow of

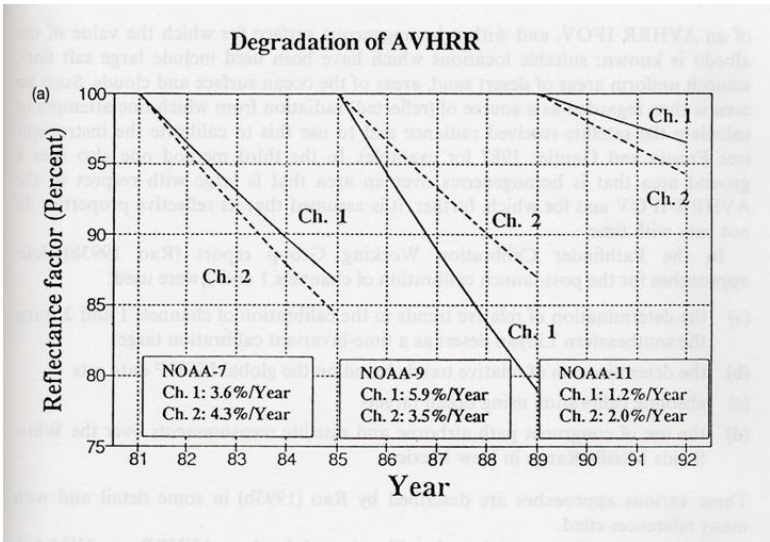

Figure 2.3: Relative degradation rates of the solar channels of AVHRR onboard of NOAA-7, -9 and -11 [13].

the earth at spacecraft sunrise. Solar contamination can introduce an error of about $0.5K$ for the 3.7 μm channel and about $0.25K$ for thermal infrared channels. Secondly, the thermal inertia of PRTs and nonlinear relationship between mean ICT temperature used for calibration and the individual temperature reported by the PRTs introduces uncertainty about the thermal state of ICT [17].

d. Inter-satellite calibration: AVHRR/2 instrument is mounted on both the NOAA-9 and NOAA-14 satellites. But the information derived from these instruments is not directly comparable because two instruments can never be identical. Also observation geometry and degradation rate of sensor could differ from each other. Hence intercalibration is indispensable if the satellite data is to be used for long-term trend analysis or climate studies [13].

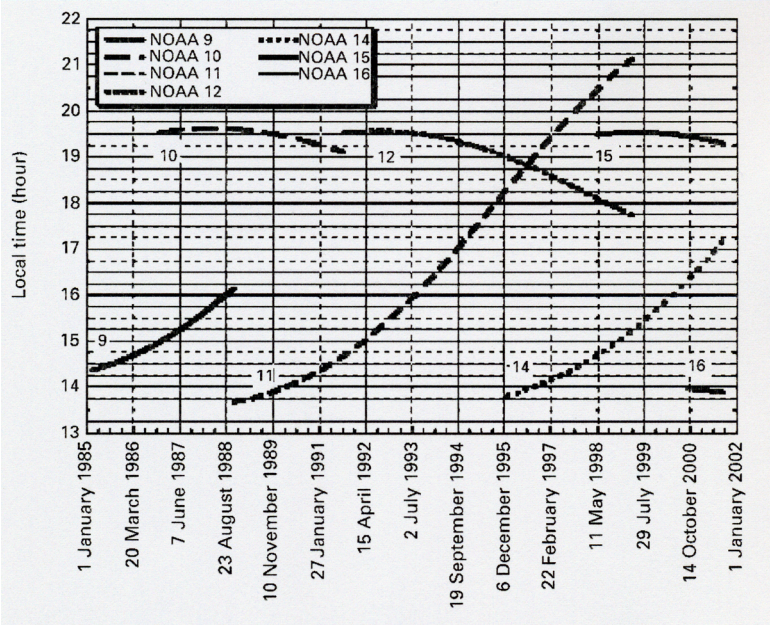

Figure 2.4: Changes in equatorial crossing times of NOAA satellites since 1985 [16].

2.3 How are these problems handled?

Most recent post-launch calibration coefficients for NOAA-9 (given in [13]) and for NOAA-14 for visible channels of AVHRR take into account degradation. Inter-satellite calibration is performed for the thermal channels in this study. Thus the first and fourth problem is taken into account. Averaging over the huge amount of day-time data (for 4 years) would suppress or dampen the effect of the third problem. The thermal channels can show noise in the observed brightness temperatures because of the inconsistency in the ICT and PRT measurements. So the observed noise is compared to the Noise Equivalent Temperature Difference limit (NEdT limit) which is a representative of the limit of noise for channels 4 and 5 of NOAA-9 and -14. For all the values of the brightness temperatures ($200K$ to $350K$), the noise

is found to be within the specified NEdT limits (see Appendix A) [Jerry T. Sullivan, NOAA, pers. communications, 2004].

A novel approach of using melting sea ice is used to monitor the thermal channel stability. During the sea ice melt, surface temperature is very close to $273.15K$. If calibrated accurately, thermal infrared channel measurements should come close to this temperature. Two regions in the Kara Sea were selected where sea ice melt starts in June every year (Fig. 2.5). The onset of sea ice melt over these 2 regions can vary each year. For example, it was June 7 in the year 1998, while it was June 3 in the year 2000. In the last few days of June, ice might melt considerably forming a small pond. A cloud detection algorithm may flag some of the days as cloudy or mixed. So, in all, between 7 to 20 days in June were available for the analysis. The Fig. 2.6 displays mean temperature from AVHRR onboard two different satellite platforms (NOAA-9 and NOAA-14) for the month of June for both regions in the Kara Sea over a study period of eight years. The thermal channels are found to be stable enough and are able to reproduce the melting sea ice temperatures with an accuracy sufficient for our study, if CTT changes surmount $1.0K$.

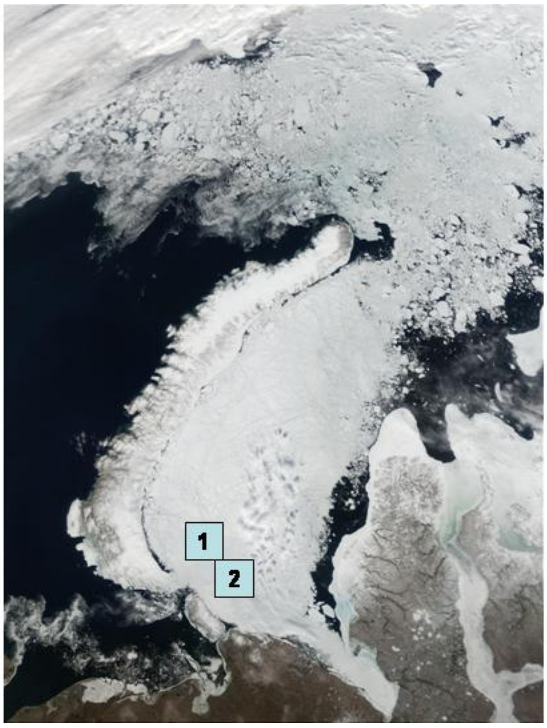

Figure 2.5: The MODIS image of the day 2 June 2002 showing two regions (R1 and R2) in the Kara Sea, where stability analysis of the thermal channels of the AVHRRs is performed. The regions are 1x2 degrees in size with the coordinates of top left corner at (72.5N, 57.5E), and (71.5N, 60.0E) respectively.

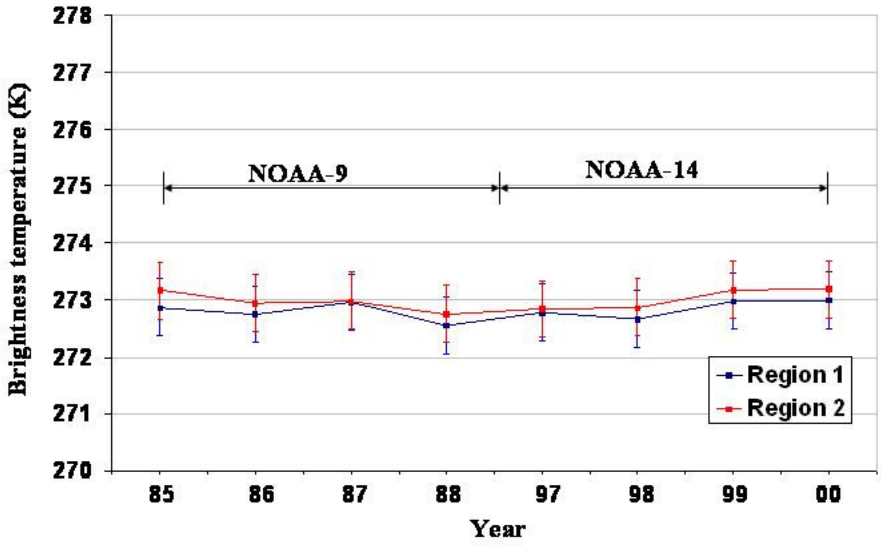

Figure 2.6: Channel 4 brightness temperatures of melting sea ice averaged for the month of June over two regions in the Kara Sea. GAC data for 8 years from NOAA-9 and NOAA-14 are used to assess the stability of thermal channels.

2.4 Atmospheric correction, cloud detection and related uncertainties

Reflectances from solar channels are corrected for the atmospheric influence. The reflectances are corrected for Rayleigh scattering and ozone absorption. The data from Total Ozone Monitoring Spectrometer (TOMS) is used to get the ozone optical thickness. Details of this procedure are described in [18] and [19]. The eccentricity of the earth's orbit and its effect on solar illumination is taken into account. These corrected reflectances and brightness temperatures along with other parameters are given as input to the cloud detection algorithm. An algorithm known as Clouds from AVHRR Phase-1 (CLAVR-1) [20] is implemented for the detection of cloudy pixels and cloud type (see Appendix B). CLAVR-1 is a hierarchical decision-tree based cloud detection algorithm which employs a series of tests that use thresholds and exploit heterogeneity of clouds. It also makes use of spectral signatures of clouds in all five channels of AVHRR. The algorithm is very robust and also has been used in the PAL data set.

Two major possible error sources are investigated here before the trend analysis: the error introduced by assuming that the brightness temperature (channel 4) is representative of cloud top temperature and the potential impact of orbital drift of NOAA-9 and -14. The first assumption is based on the fact that cloud emissivity in this spectral range is nearly equal to 1 (for optically thick clouds which are analysed in the study) and brightness temperatures are required to be corrected mainly for water vapour (WV) absorption above clouds. So far, most of the studies were restricted in estimating WV correction for clear sky conditions in the retrieval of sea and land surface temperatures [16][21][22][23][24]. Using the radiative transfer code Streamer [25] and MODIS Level 3 WV data product shows, however, that for the chosen study area the error induced in CTTs by not applying WV correction would be less than $0.5K$ for thick low clouds and would be

very small ($< 0.2K$) for high convective clouds. This error would even be less for the winter season.

The foremost impact of orbital drift to a later afternoon overpass is a change in solar zenith angle resulting in a cooling trend [16] [24]. However, the error induced because of orbital drift should be small in this study because there are smaller daily solar zenith angle changes in higher latitudes resulting in smaller time rates of temperature change [24]. Hence, this effect will be smaller over the study area with latitudes above 48.5N. Further, this effect would even be smaller for winter season. Since the winter and summer seasons are analyzed separately and similar thermal signatures have been found, this is an indication for a small drift influence. In addition NOAA-9 during 1985-88 and NOAA-14 during 1997-2000 showed similar changes in equator crossing times, further reducing the potential impact of this effect. Considering both the effects together, the error involved in the present analysis will be less than $1K$.

2.5 Validation

Calibrated reflectances and brightness temperatures are validated using the PAL data set [18] and the thermal infrared channels of the MODIS sensor on the Terra satellite [9]. Three different validation sites, in Europe, China and USA, are selected and PAL and GAC data sets for any single day, chosen randomly, are processed and compared. Correlation for all the channels in all cases between GAC and PAL data sets is found to be larger than 0.90. Histograms of frequency distributions for visible and thermal channels for GAC and PAL also showed nearly identical signatures (Figs. 2.8 and 2.9). Further, we used MODIS channel 31 ($10.78 - 11.28\mu m$) and channel 32 ($11.77 - 12.27\mu m$) differences to confirm the thermal channel differences of AVHRR. Although the bandwidth of these MODIS channels is narrower than for AVHRR, they lie in the same spectral range. Scatter plots of calibrated AVHRR GAC brightness temperatures showed similar behaviour as MODIS

for three randomly selected cases.

The cloud top temperatures (CTTs) are validated using MODIS Level 2 Cloud product. Correlation between GAC CTTs and MODIS CTTs have found to be greater than 0.90 for all the 10 randomly selected cases studied. As an example, scatter plot of CTTs is shown below (Fig. 2.7) for the day 122 of year 2000 over the study area of Europe.

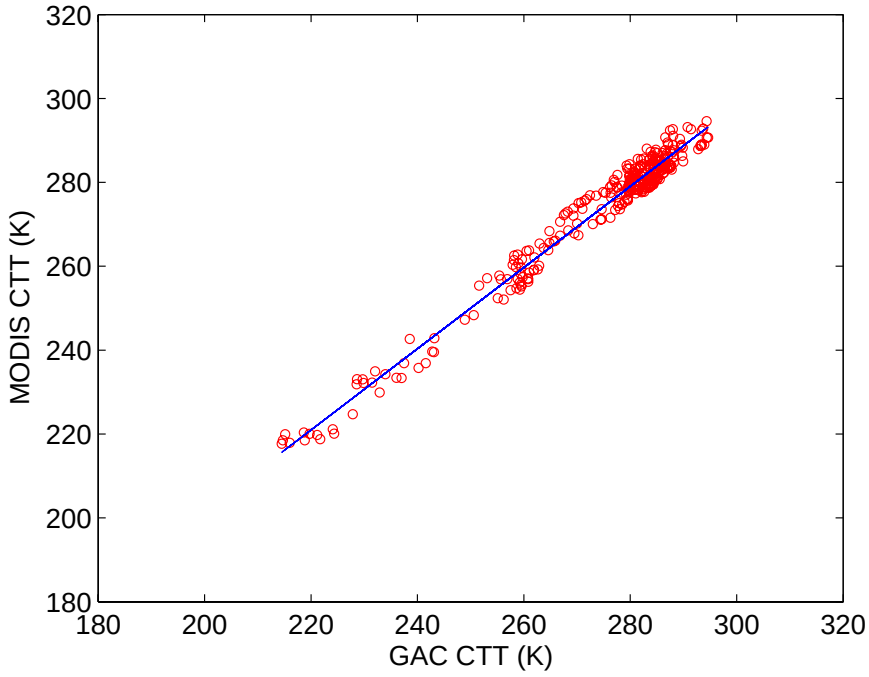

Figure 2.7: Scatter plot showing correlation between GAC and MODIS derived CTTs for day 122 of year 2000 for a test area over Europe.

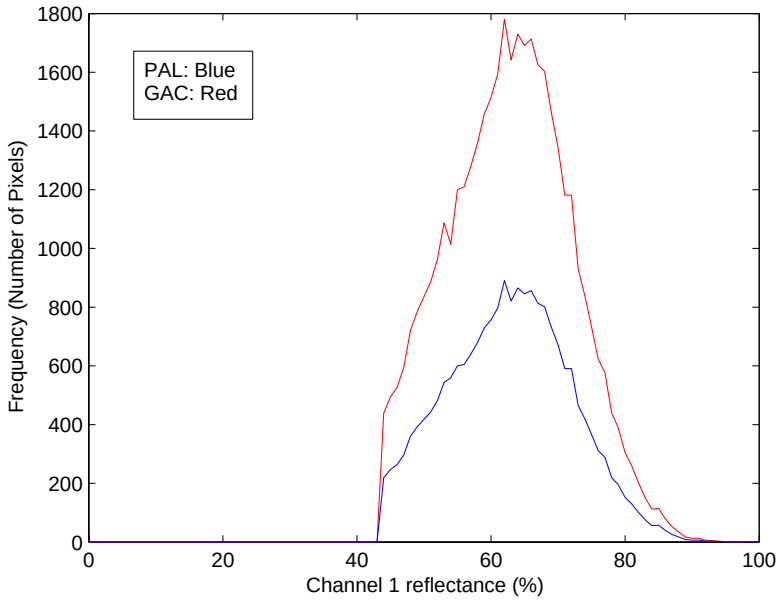

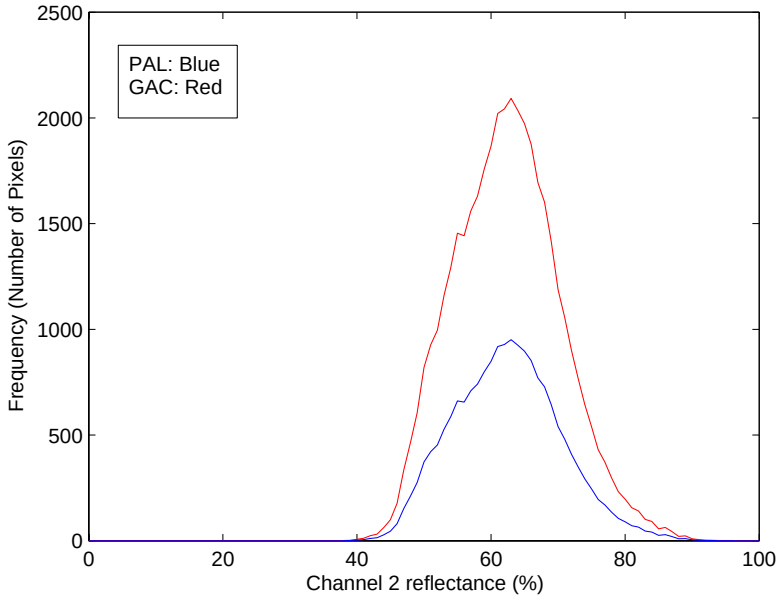

Figure 2.8: The PAL and GAC data show similar frequency distributions for the solar channels of the AVHRR for the month of May 2000 for a test area in north Europe. Note that due to different binning and resolution for the PAL and GAC, the total number of pixels are not equal.

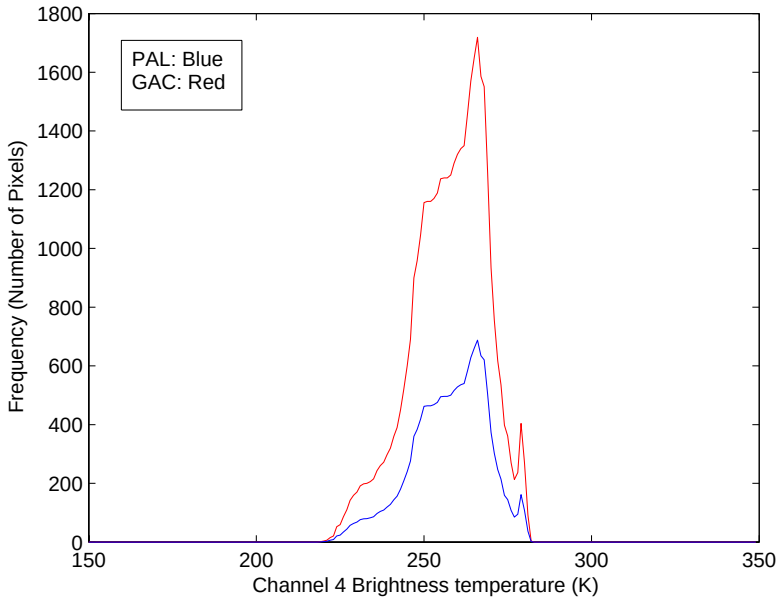

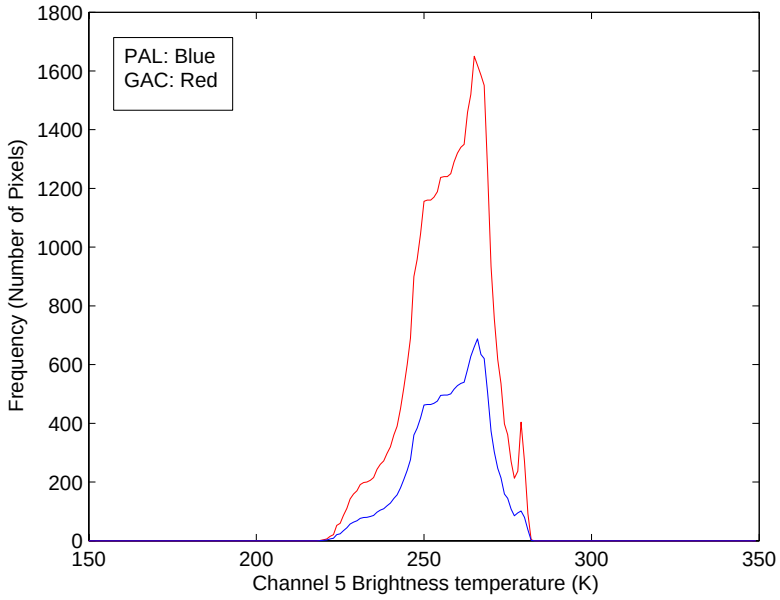

Figure 2.9: -same as Fig. 2.8 but for thermal channels

Considering all the aspects of potential errors described above, it can be summarised that an accurate and robust procedure is developed (in ANSI C language) for the processing of AVHRR GAC level 1b data. It can be used with little modifications to evaluate and analyze not only cloud physical properties but also other parameters like surface albedo, sea surface temperature (SST), Normalized Difference Vegetation Index (NDVI) etc from long-term satellite data for different regions of the globe. In the next chapters, this software is used to evaluate cloud properties.

Chapter 3

Change in cloud top temperatures over Europe

3.1 Air pollution over Europe

Enormous amounts of pollutants had been emitted in the atmosphere in Europe, particularly by the industries and power plants in Eastern Germany, Poland and the Czech Republic in the late 1980s. Economic growth of central and eastern European countries was driven by the growth in heavy industries which demanded high energy and power that was supplied mostly from coal fired power plants. For example, emissions from power plants in the former German Democratic Republic (GDR) accounted for almost 50 percent of total emissions of primary particulate matter (PPM). In the western part of Germany the annual emissions of PPM were $0.4-0.6 Tg/yr$ during 1985-1989, while the values for the eastern part were four times higher, reaching $2.2-2.5 Tg/yr$. According to European Monitoring and Evaluation Programme (EMEP), also the formation of secondary inorganic aerosols was a major contributor to air pollution over Central Europe in the late 1980s [26][27].

In Poland, heavily industrialized parts like Krakow and Kattowice are the most polluted ones. The city of Krakow was rated as the third highest in particulate matter (PM) concentration, with an annual emission of $10,900t$

in the year 1997. For the same year the annual emission of polluting gases was $103,400t$, including $26,900t$ for sulphur dioxide (SO_2) alone. Annual SO_2 emissions were more than 7 million tons in the former GDR, 4 million in Poland and 2 million in the Czech Republic in the late 1980s [27].

After the collapse of the East-Bloc and the fall of the Berlin Wall in 1989, the changes in political and economic scenarios lead to major changes in industrial activities resulting into strong reduction in air pollution in some countries. Details of emissions for these countries are shown in Fig. 3.1. Such strong changes in pollution levels definitely had an impact on cloud properties. The episode with very high pollution (1985-88) and with low pollution (1997-2000) seemed ideal to study the influence of air pollution on cloud properties. Due to decrease of aerosol precursor gases, a pronounced decrease of cloud albedo of about 2 percent from the late 1980s to the late 1990s is observed [26]. During winter in source regions of anthropogenic particulate matter emissions the cloud reflectance was more than 5 percent lower referring in addition to an absorption effect caused by black carbon in clouds [26]. In these main European emission areas the high degree of air pollution generally enhanced the variability of cloud reflectance during the 1980s [27]. The changes in cloud top temperatures (CTTs) and variability could give further insight into aerosol indirect effects. Therefore the thermal range is evaluated here using long-term satellite measurements.

3.2 Changes in cloud top temperatures

To assess changes and variability in CTTs, two four-year episodes, one in the late 1980s (1985-1988) and another in the late 1990s (1997-2000) are evaluated. Four years in each episode are used for statistical analysis to strongly reduce the influence of interannual variability. These episodes are not only representative of high and low pollution load [26][27] but also are largely free of volcanic aerosols in the stratosphere. Two 4 months periods, summer (May, June, July and August) and winter (November, December, January

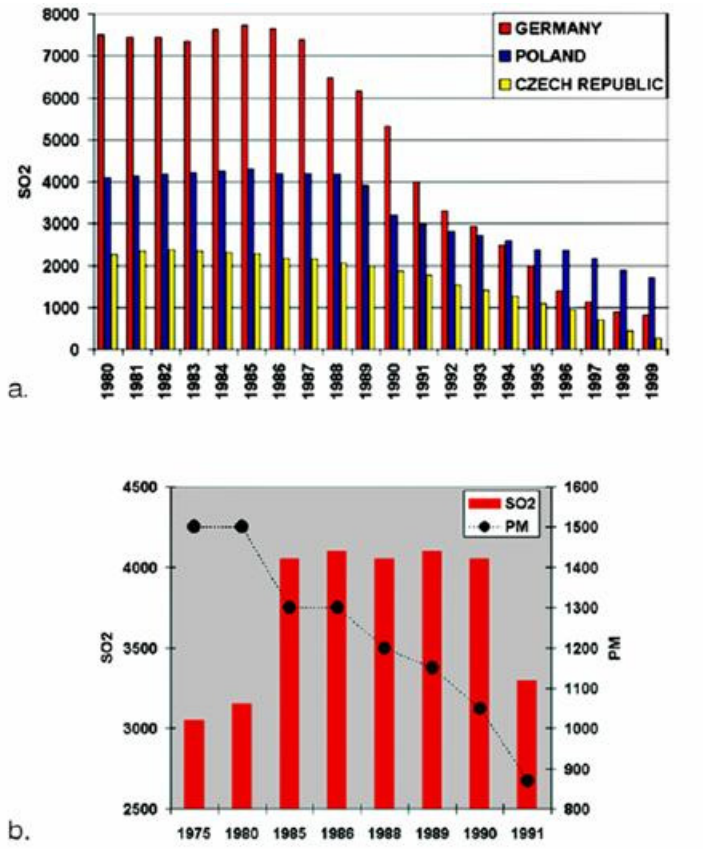

Figure 3.1: a) Annual sulphur dioxide (SO_2) emissions in Germany (including the former GDR), Poland, and the Czech Republic, in kilotons for the period 1980-1999, according to the EMEP database b) Annual emissions of particulate matter (PM) and sulphur dioxide (SO_2) for power plants in the area of the former GDR, in kilotons. Data are from the German Environmental Agency [27].

and February), for each episode are analyzed separately as the height of the atmospheric boundary layer and temperature influence on concentration of pollutants differs most for these months. Data over both sea and land are evaluated, since continental clouds are affected stronger by the pollutants. Furthermore continental clouds are divided into two groups, namely, clouds over polluted regions and comparably remote regions. The regions where cloud albedo is less than 60 percent in winter season are considered as polluted regions [26]. Daytime GAC data and only those pixels classified as

cloudy by the CLAVR algorithm are used for analysis. Channel 4 brightness temperature is used as a representative of CTT. An identical analysis was performed for channel 5 as well.

Emphasis is given on low and medium level clouds as in [26], but additionally also convective clouds are considered. Here, convective clouds are cloudy pixels with the cloud flag of 11 from CLAVR-1 algorithm after undergoing series of contrast, spectral and spatial tests (refer Appendix B for cloud flags). These clouds are likely to be influenced by anthropogenic aerosols as well. The astonishing results (for summer season) for low and medium level clouds (LM) and for low and medium level plus convective clouds (LMC) over land (L), sea (S) and polluted regions (P) are tabulated in Table 3.1. All cloud types over all surface types had lower brightness temperatures during higher pollution levels. Low and medium clouds over land in the late 1980s were colder by $2.1K$ compared to the late 1990s. The temperature drop is not so strong over sea with $1.3K$ but stronger in polluted regions where average CTT was $2.9K$ lower. When convective clouds are added to the low and medium clouds the changes become strongest, reaching $-4.4K$ over land and $-4.9K$ over polluted regions. Analysis for only convective clouds over land shows that clouds were colder by $4.8K$ and over polluted regions by $5.2K$ in summer.

Similar trends have been observed for winter for LM, LMC and also when only convective clouds were considered. For example, CTT change reached $-1.9K$ over land and $-2.5K$ over polluted regions for LM clouds. When convective clouds were also considered this change in CTT reached up to $-3.7K$ over land and $-3.9K$ over polluted regions. The CTT changes using channel 5 also show nearly identical trends for LM, LMC and convective clouds, confirming the observed changes in channel 4. Fig. 3.2 shows the spatial pattern and magnitude of these changes over study area for LMC clouds in summer season.

Can such pronounced changes in CTTs be explained by changes in pollution levels over this area during these two episodes? Or can the hypothesis

Table 3.1: Cloud top temperatures and their changes (in K) for two 4 year periods for low and medium clouds (LM) and convective clouds added (LMC) over land (L), over sea (S) and over pollution centres (P) for summer.

Summer		1985-88	1997-00	Difference
LM	L	258.9	261.0	-2.1
	S	262.6	263.9	-1.3
	P	257.9	260.8	-2.9
LMC	L	255.6	260.0	-4.4
	S	261.8	263.4	-1.6
	P	255.2	260.1	-4.9

that the increase in aerosol load, in particular fine aerosols from anthropogenic pollution, lifts clouds and thus decreases CTTs and induces stronger variability over and around areas of pollution sources be confirmed?

To assess the validity of the hypothesis, firstly, a statistical analysis using the coefficient of variation is performed. The variability in CTTs for LMC is much higher in the late 1980s compared to the late 1990s. Fig. 3.3a shows the coefficient of variation (in thousands) for low and medium level plus convective CTTs for summer in the late 1980s and Fig. 3.3b for the late 1990s. In the late 1980s, highest variability occurred over and around polluted regions of Poland, Germany and the Czech Republic (so called Black Triangle). Even during the late 1990s, an area around the industrial zone of Poland (i.e. Krakow and Kattowice) still shows the highest variability. Similar results have been documented in [26] for variability of cloud albedo. In the 1980s, particulate matter, aerosol precursor gases like sulphur dioxide (SO_2) and nitrogen oxides (NO_x) have been emitted into the atmospheric boundary layer in huge quantities from power plants, district heating, commercial, industrial and residential combustion, road transport and coal extraction and refining over Europe. In Poland, emission load was very high over urbanised cities like Krakow and Kattowice. After the end of the East Bloc in 1989, changes in politics and economy lead to a considerable decrease of emissions

during the 1990s. For example, SO_2 emissions decreased by about 50 percent in Europe from $49Tg$ in 1988 to $26Tg$ in 1998 [27].

Secondly, the trend in minimum CTTs for these two episodes is analysed. Figs. 3.4a and 3.4b show the absolute minimum CTT that occurred during each day in summer and winter of the late 1980s and the late 1990s. Linear regression clearly indicates that during the late 1980s (shown in blue colour) highest cloud tops were colder. In a significant number of cases, these minimum CTTs are observed over polluted regions of central and eastern Europe for both episodes.

And finally, regions of observed CTT changes coincide with regions where the strongest modelled influence of anthropogenic particulate matter is seen [28] and black carbon emission inventories show highest values [29, 30]. All these investigations point to CTT changes caused by pollution over Europe. This observed indirect aerosol effect in the thermal infrared on regional scale could be equally important but of opposite radiative forcing, and it might be dominant over the solar radiation changes. Thus it needs to be further investigated and also for other regions.

3.3 Summary

CTTs over central and eastern Europe are analysed for two four-year episodes during the late 1980s and the late 1990s using long-term satellite measurements. Tops of low and medium level clouds were colder by more than $2K$ and by $4K$ if convective clouds are included during the late 1980s compared to the late 1990s. Stronger variability in CTTs is also seen during the late 1980s. A further support for pollution as the cause of CTT changes comes from a higher impact over metropolitan areas and industrial centers. All these changes are not contradicting concomitant changes in pollution characteristics over Europe during these two episodes, suggesting that there is an indirect aerosol effect in the thermal spectral range as well.

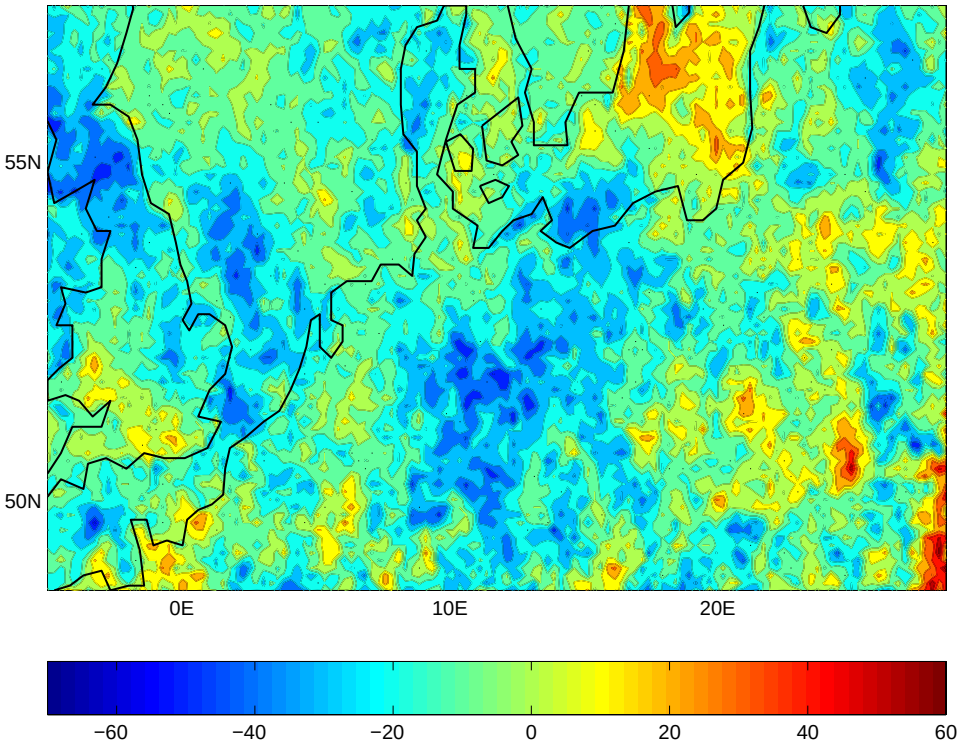

Figure 3.2: Changes in LMC cloud top temperatures (in Kx10) from the late 1980s to the late 1990s for summer season.

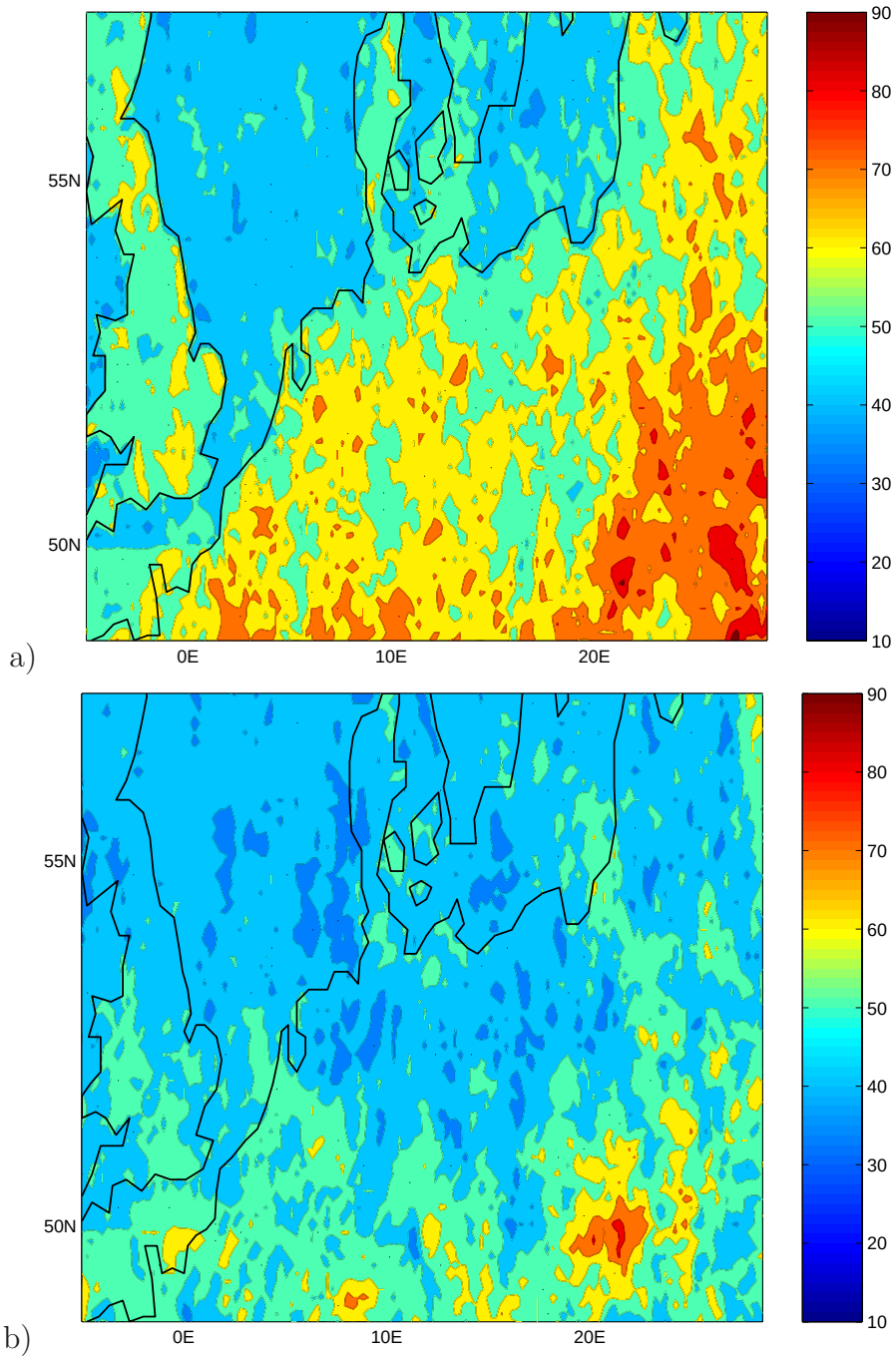

Figure 3.3: Coefficient of variation of brightness temperatures (in thousands) for low and medium level plus convective clouds for the late 1980s (a) and for the late 1990s (b). Lower-left coordinates of study area are (48.5 N, 5.0 W) and upper-right are (57.5 N, 28.5 E). Strongest variability occurs in (a) over polluted regions in Poland, Germany and the Czech Republic [44].

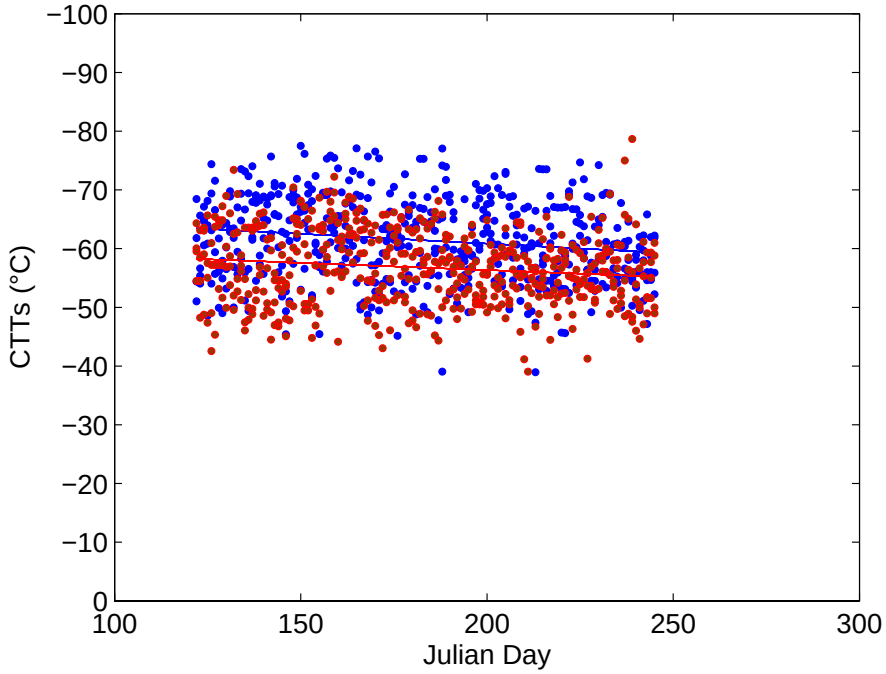

a)

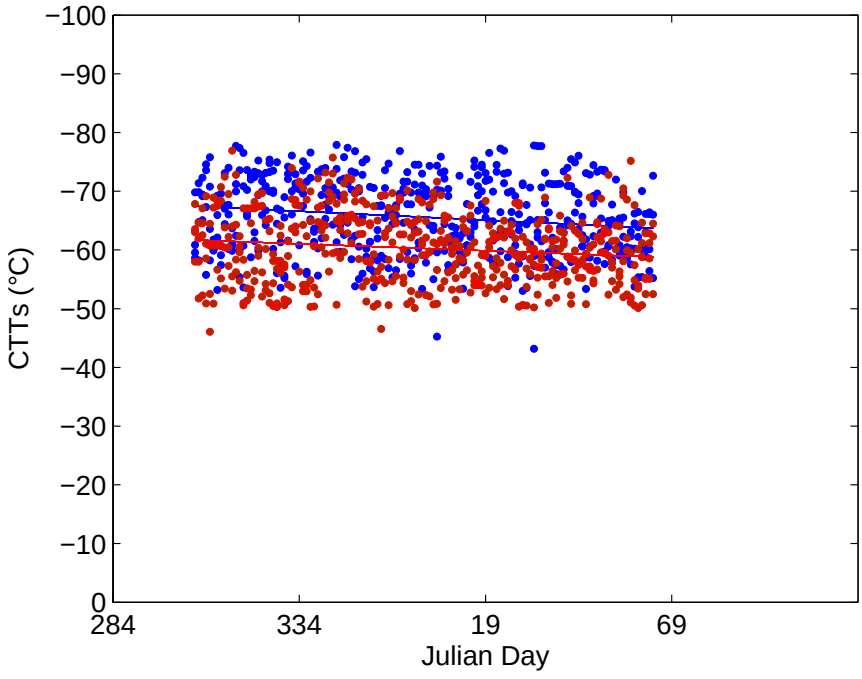

b)

Figure 3.4: Absolute minimum cloud top temperatures (CTTs) over Europe in degrees Celsius for each day in a) summer, and b) winter of the late 1980s (blue) and the late 1990s (brown). Linear regression clearly shows the lifting of cloud tops in the late 1980s.

Chapter 4

Impact of ship emissions on cloud properties over coastal areas

4.1 Overview of ship emissions

The principal emissions from ships include exhaust gases, hydrocarbons and particulate matter. Ship emissions are one of the least regulated sources of air pollution. Regionally, this could have an impact on the atmosphere, radiation and hence on climate. According to an International Maritime Organization study [31], global ship traffic density share reaches 85 percent in the northern hemisphere. EMEP estimates that the contribution of secondary inorganic particles formed from ship emissions in western European coastal areas varies between 20-30 percent. Several global inventories for the energy/fuel consumed by shipping are available [32][33][34]. The most recent inventory [35] estimates a fuel consumption of approximately 280 million metric tonnes (Mt) for the year 2001 compared to $64.5Mt$ in 1950. When compared to other modes of transport (i.e. aviation and road traffic), this fuel consumption is 16 percent, but due to the differences in engine exhaust ship emissions significantly contribute to pollutants.

Ship based trade and activities, and thus emissions continue to grow, while land based pollution from industries is partly decreasing, particularly in Europe. SO_2 emissions in European seas will increase by almost 45 percent by the year 2020 [36]. From the year 2015, SO_2 emissions from shipping in Europe are projected to exceed those from land. About 90 percent of all ship emissions in the North Sea originate from within $90km$ from the coast line (Fig. 4.1). These ship emissions could have an impact on the cloud properties over coastal areas as they can be additional sources of cloud condensation nuclei (CCN). There are only few studies that use remotely sensed data to analysed this impact and most of them are limited to studying microphysical properties of clouds or changes in CCN and/or restricted to episodes [37][38][39][40][41]. In this context, satellite data for six years from NOAA-14 is evaluated to assess the possible impact of these ship emissions on coastal areas in Europe. The study area is chosen in such a way that it covers English Channel and Europe's top three polluting harbours, namely Rotterdam, Antwerp and Milford Haven.

4.2 Evaluation of cloud properties

Cloud albedo and cloud top temperature are evaluated in this case study. AVHRR GAC level 1b data from NOAA-14 is used and processed as described in chapter 2. Summer (May, June, July and August) and winter (November, December, January and February) seasons from 1997 to 2002 are analysed. The study area is divided into 3 zones, namely coastal zone (CZ), sea zone (SZ) and land zone (LZ). The CZ is approximately $50km$ area on either side of the coast line (defined by the $1km$ resolution land/sea mask). The area landwards is categorized as LZ and seawards as SZ. The idea was to separate the CZ from LZ and SZ so as to analyse the cloud properties of all the three zones individually, since this $100km$ area along the coast is most likely affected by ship emissions due to high ship traffic density and shipping activities like harbouring. Only low level clouds are analysed since they are

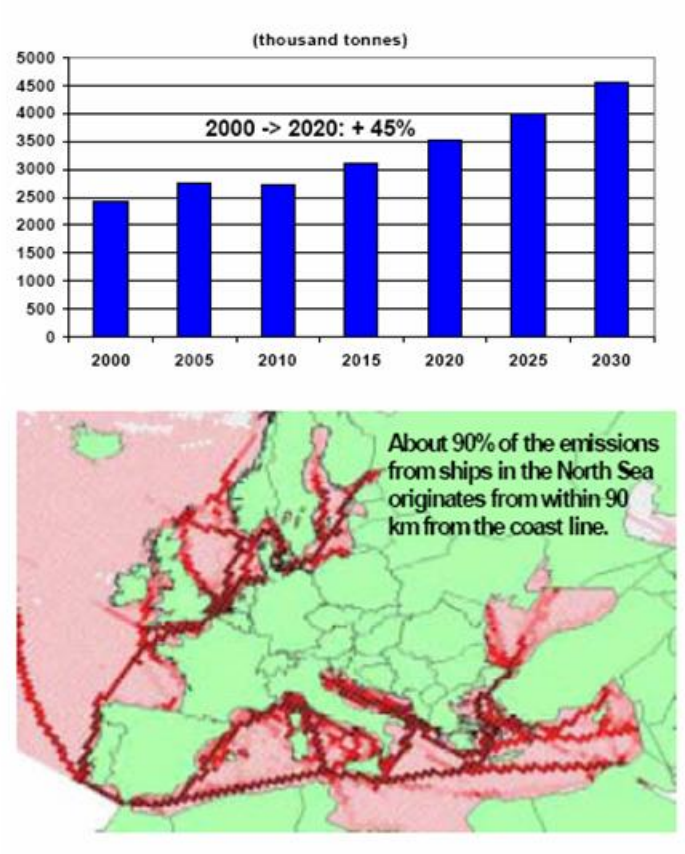

Figure 4.1: a) Projections of SO_2 ship emissions for European seas. b) Coastal areas in Europe with ship activities [36].

most likely to show an impact from ship emissions.

Results (Fig 4.2) indicate that there are changes in cloud properties (monthly averages) over CZ. The albedo over CZ is increasing, while albedo over LZ shows a decrease. On the other hand, the cloud top temperatures (CTTs) over CZ are decreasing and increasing over LZ. Such behaviour of albedo and CTT over CZ and LZ can be explained by decreasing air pollution over land and increasing ship emissions. The slight increase in albedo and decrease in CTT over SZ could be due to a weakening but still with less ship traffic detectable influence of these emissions over sea areas. The first indirect aerosol effect, the Twomey effect, seems to exist for CZ and LZ in

the solar spectral range, and also the thermal effect (presented in this thesis).

To validate this interpretation, firstly, we analysed the aerosol optical thickness data (at $670nm$) from Aerosol Robotic Network (AERONET, Level 2.0 quality assured and manually inspected) [42] and EMEP Expert Emissions (EMEP-EE) [43]. There are two AERONET stations that fall into our study area and have a record of aerosol optical thickness for more than 3 years. Fortunately, one falls into LZ (station at Lille, France) and the other is close to CZ (station at The Hague, Netherlands). The EMEP-EE for the UK, Netherlands, France, Belgium, North Sea and north-east Atlantic ocean are also analyzed. The trend is shown in Figs. 4.3 and 4.4. Aerosol optical thickness for the station (Lille) in LZ and the SO_x emissions from EMEP-EE for all countries confirm decreasing trend in air pollution. A similar decreasing trend from EMEP-EE for all the main pollutants is seen over these countries. But the station (The Hague) closest to the CZ and EMEP-EE for sea areas show an almost constant or slightly increasing trend (in the case of the north-east Atlantic Ocean).

Since the impact of ship emissions could be more localised, four smaller regions in the study area are selected and trends in cloud properties are observed there (refer Fig. 4.6 for selected 4 regions). Region 1 covers an area in and around harbour Milford Haven, region 2 part of the English Channel, region 3 areas in and around the harbours Rotterdam and Antwerp and region 4 is chosen in the open ocean, away from the coast. Observed trends in cloud albedo and CTTs are shown in Fig. 4.4. Regions 1, 2 and 3 show a sharp increase in cloud albedo and decrease in CTTs compared to region 4. Rotterdam is the most polluting harbour in terms of NO_x, SO_x and particulate matter, followed by Antwerp and Milford Haven. For example, estimated annual emissions of SO_2 from Rotterdam are $3.7kT$, followed by $2.2kT$ for both Antwerp and Milford Haven for the year 2000 [36]. The English channel is the busiest sea route for almost all types of ships. These ship emissions are increasing and also predicted to increase further in future. All the aspects above do point to a possible impact of these emissions on

cloud properties.

Final confirmation comes from the analysis of variability of cloud properties in the study area (see Fig. 4.6). High variability induced by the pollution is seen for both cloud albedo and CTTs over these harbours and the coastal areas. All the trends and variability observed in cloud properties because of air pollution are in line with the finding in [26] and [44], where changes in cloud albedo and cloud top temperatures are studied as a function of air pollution over Europe.

4.3 Summary

Results of the satellite data analysis suggest an influence of ship emissions on cloud albedo and CTTs over coastal areas. It also confirms the fact that there is an indirect aerosol effect in the thermal range as well. Ship emissions need particular attention in assessing the cloud properties over coastal areas and could even be significant as shown in this study. This would directly have an impact on the climate of coastal areas. Various studies involving ship emission inventories and precise chemical transport models for such areas are important to further validate such an impact on local or regional scales. Remote sensing information at higher resolution from recent more sophisticated sensors like MODIS, POLDER, MERIS, SCIAMACHY etc could give more insight in this context.

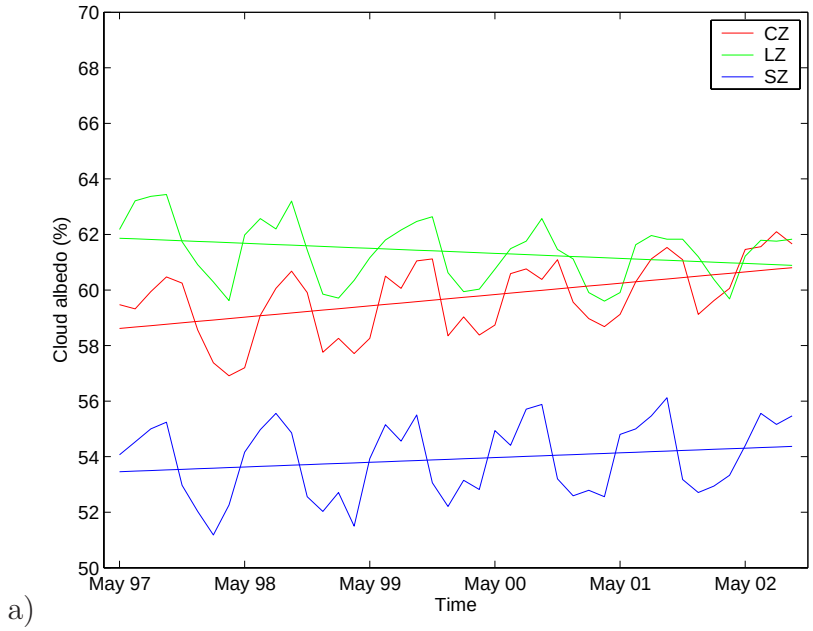

a)

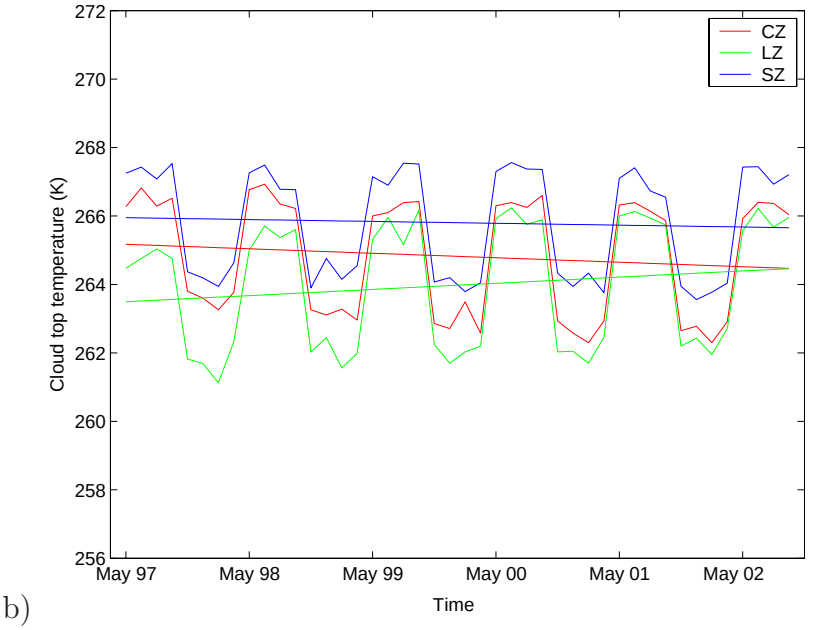

b)

Figure 4.2: Observed changes in cloud albedo (a) and in cloud top temperature (b) from May 1997 till August 2002 (monthly averages, in cycles of summer and winter) over the study area. Increase in cloud albedo and decrease in CTT over coastal zone (CZ), and vice versa for land zone (LZ) suggest an impact of ship emissions [45].

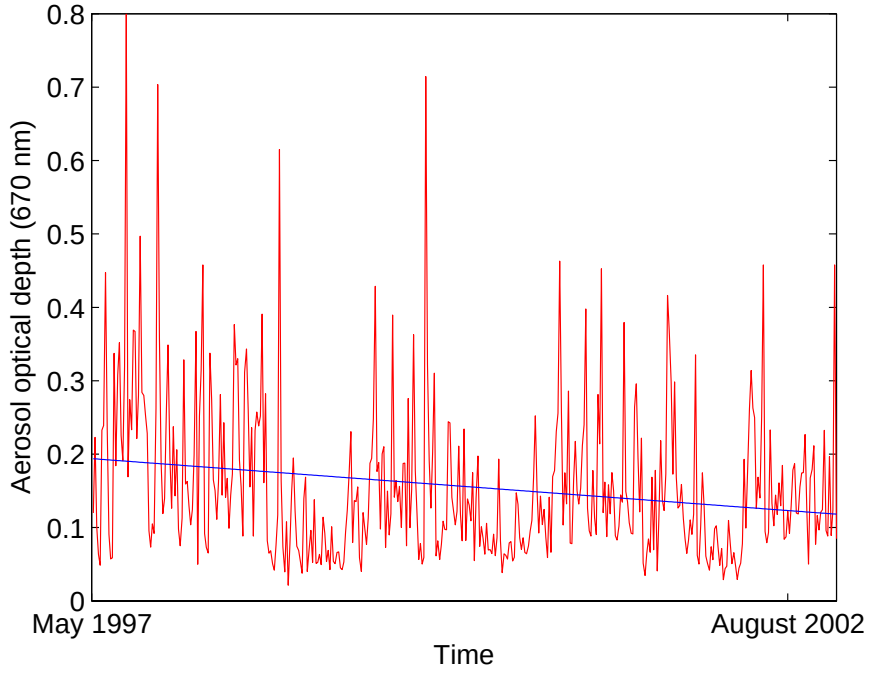

a)

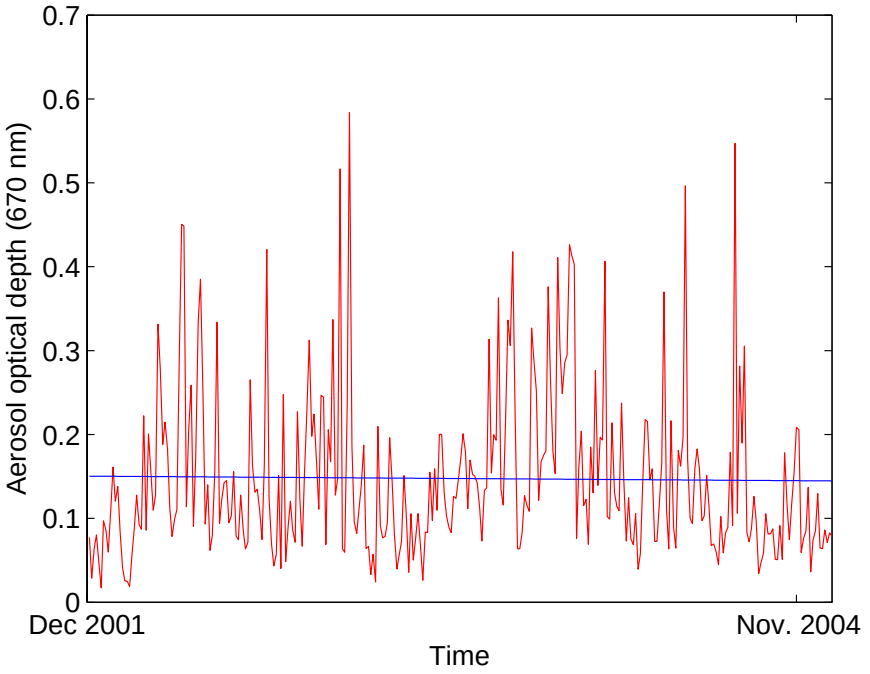

b)

Figure 4.3: Aerosol optical thickness data from 2 AERONET stations (a) Lille, and b) The Hague) confirm the decreasing pollution over land and almost constant trend for the coastal areas.

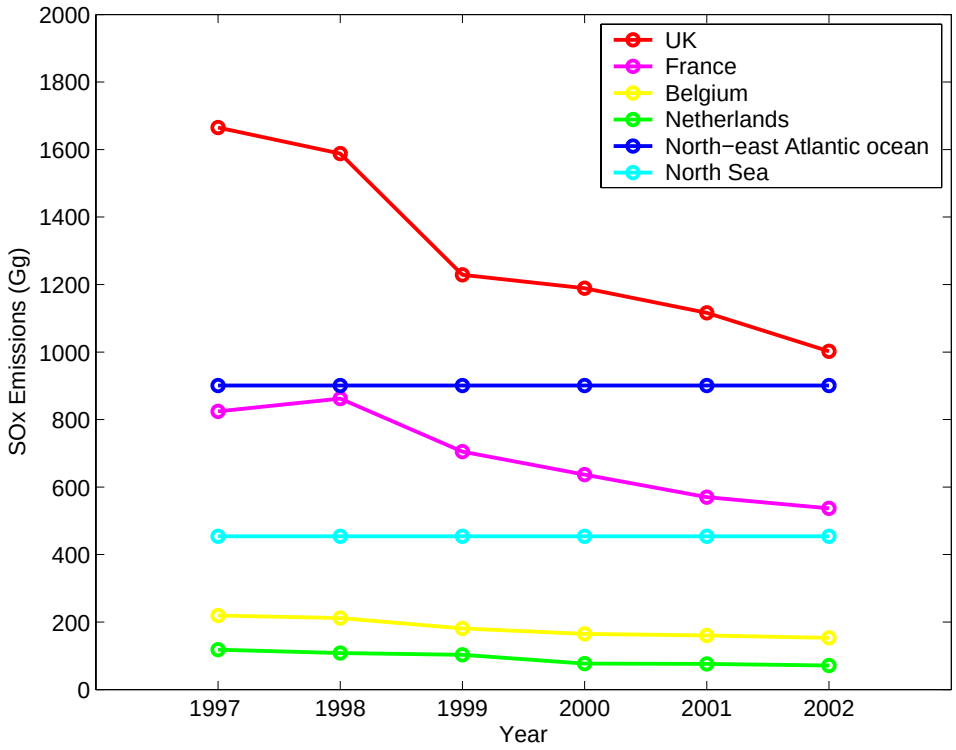

Figure 4.4: EMEP Expert Emission data for four countries and two sea areas confirm the decreasing pollution over land and almost constant or slightly increasing trend for the sea areas.

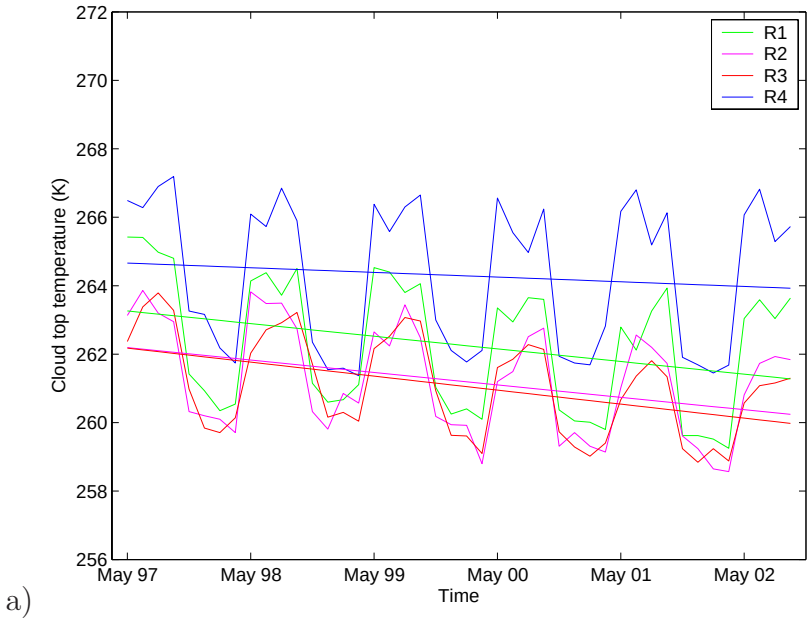

a)

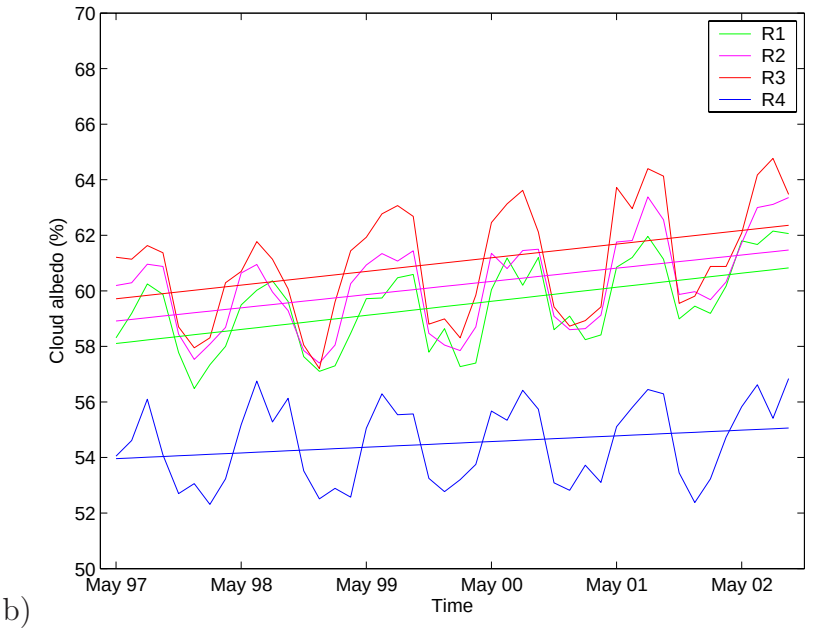

b)

Figure 4.5: Trend observed in cloud albedo (a) and CTTs (b) for 4 regions from May 1997 till August 2002 (monthly averages, in cycles of summer and winter) covering 3 harbour areas (R1, R3), the English Channel (R2) and a relatively remote ocean region (R4) clearly confirms the influence of ship emissions [45].

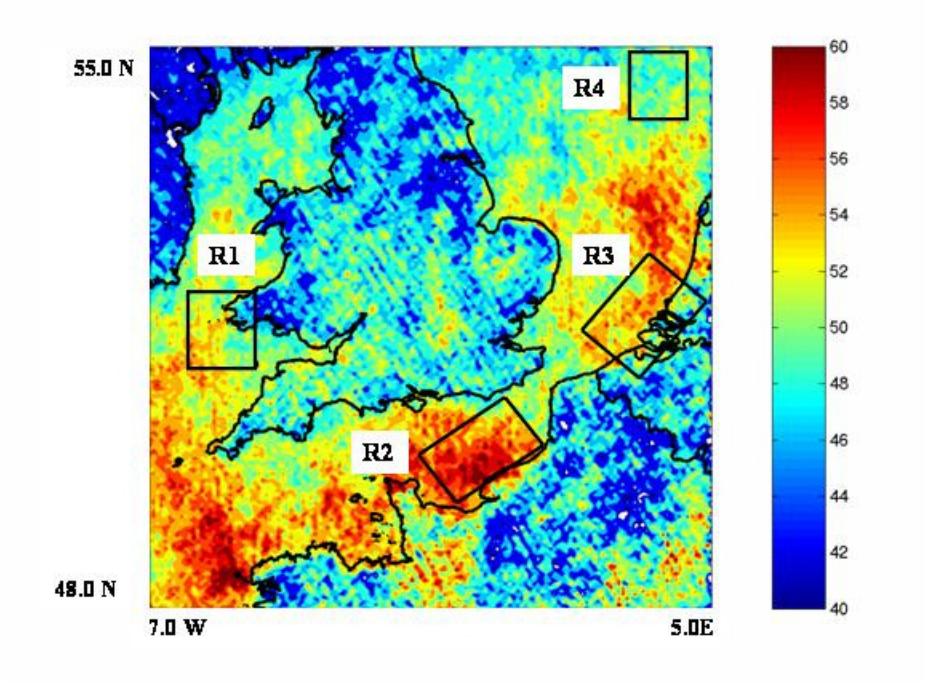

Figure 4.6: Coefficient of variation of CTTs over study area and four regions. High variability can be easily seen over harbours Milford Haven (R1), Rotterdam and Antwerp (R3), English Channel (R2) and coastal areas [45].

Chapter 5

Conclusions and outlook

A new indirect aerosol effect in the thermal spectral range is revealed through two case studies using long-term satellite data from AVHRR. Air pollution and cloud top temperatures seem to co-vary. This effect could also be equally important than indirect aerosol effects in the solar spectral range and cannot be neglected. More and more emphasis on such studies is needed to assess an impact on the global scale as this may have direct relevance to the earth radiation budget. Evidence of possible impact of ship emissions on coastal areas is also presented. Remotely sensed information from satellites could be key in further understanding of these impacts on regional and global scales.

The foremost task is to develop a procedure to correct the effect of orbital drift of NOAA satellites on measurements. Although this effect, if at all present, is almost negligible at higher latitudes, could be significant at lower latitudes. This will result in very robust data set, which could be used in investigating cloud properties of any part of the globe for the last 20 years. Then, special emphasis will be given on analysing this new indirect aerosol effect for the entire Europe and the north Atlantic ocean. Due consideration will be given to the pollution hotspots in Europe, and influence of anthropogenic pollution and Saharan dust on the north Atlantic. Impact of ship emissions on coastal areas in Baltic and Mediterrenean Sea would also be an important issue for the future. For example, Fig. 5.1 shows the difference in

low level cloud top temperatures for the entire Europe from 1980s to 1990s (for summer season). Changes in the cloud top temperatures over land and ocean are interesting and should be investigated further. Remote sensing information from AVHRR will be complemented by more sophisticated sensors like MODIS, POLDER, MERIS etc and ground based observations as well. Overall goal is to better understand the processes and minimise the uncertaintity in earth radiation budget caused by insufficient knowledge and quantification of aerosol effects on climate.

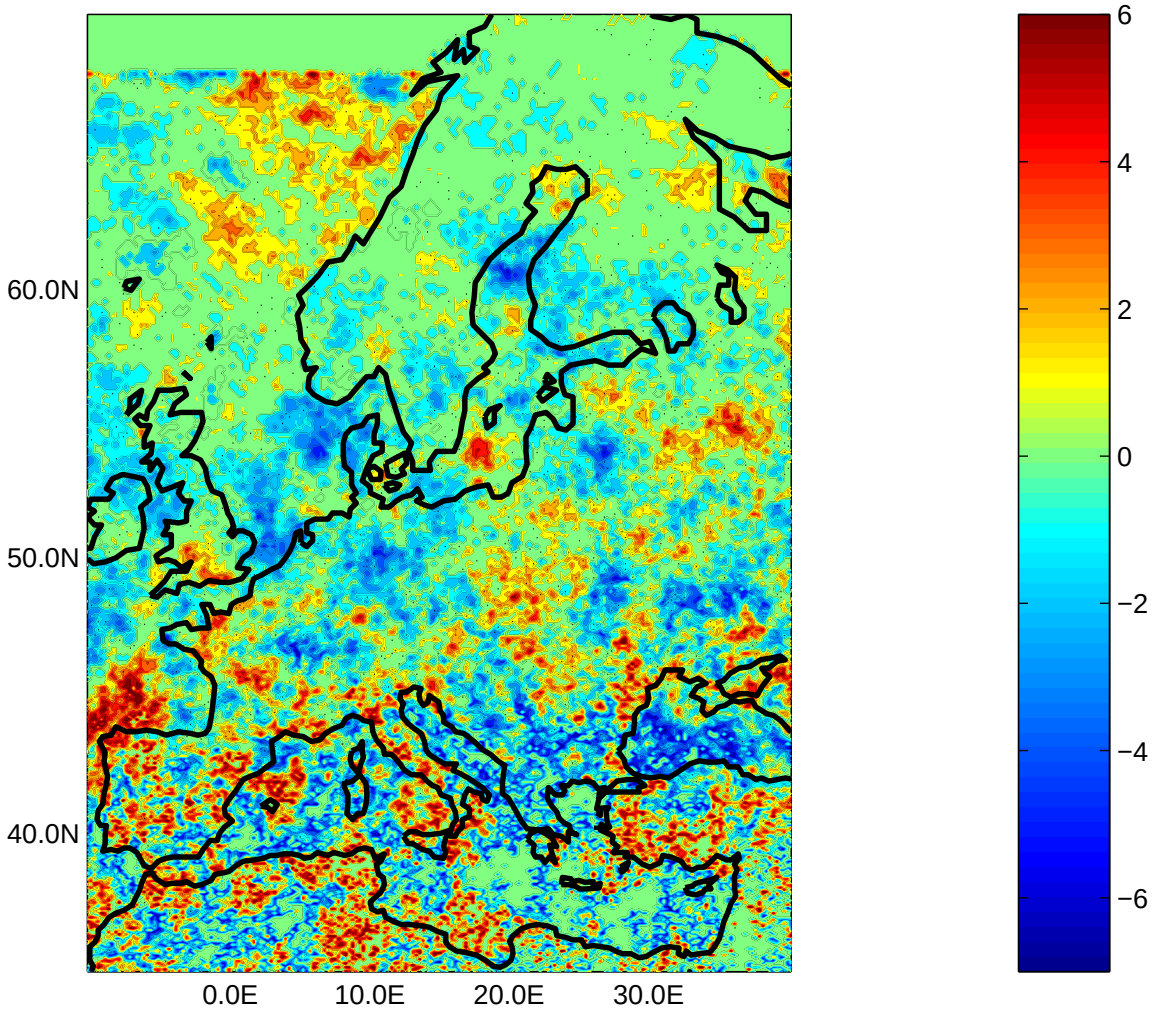

Figure 5.1: Changes in low level cloud top temperatures from late 1980s to the late 1990s for summer season (in K).

Appendix A

NEdT and its limits

The Noise Equivalent Temperature Difference (NEdT) is a measure for the noise δR of the thermal channels. It is a function of channel wavelength, gain, and temperature. It is given by

$$\delta R = \sqrt{2} G \delta C \sqrt{1 - \epsilon(1 - \epsilon)} \tag{A.1}$$

where

$$\epsilon = \frac{C_P - C_{SP}}{C_{ICT} - C_{SP}} \tag{A.2}$$

and

$$G = \frac{R_{ICT} - R_{SP}}{C_{ICT} - C_{SP}} \tag{A.3}$$

C_P, C_{SP} and C_{ICT} are pixel, deep space and ICT counts respectively for the thermal channel. G is the channel gain (radiance/count). And δC is the standard deviation of deep space and ICT counts. R_{SP} and R_{ICT} are the radiances received by the thermal channel from deep space and ICT respectively. The δR calculated with the above formulae should be less than the NEdT limits (for a given channel and temperature). The calculation of NEdT limits is out of the scope of the present study, however, an approximate procedure is given below.

Scientific basis for the approximation of NEdT limits:

In pre-launch calibration, the spectral response curves for AVHRR thermal channels 3B, 4, and 5 are measured. The responses of the AVHRR in a small wavenumber interval centered at wavenumber ν_1 is measured, then the spectral response for a wavenumber interval centered at ν_2 is measured, and so forth. For the AVHRRs, before NOAA-15, there were about 20 intervals. From the NOAA-15 AVHRR onwards, there are about 200 intervals. From the spectral response measurements, the AVHRR radiance R in each channel is computed by first calculating how much radiance the AVHRR will sense from a blackbody held at temperature T. For a blackbody at temperature T, the radiance in a small wavenumber interval around wavenumber ν is given by

$$B(T,\nu) = \frac{c1\nu^3}{e^{(\frac{c2\nu}{T})} - 1} \tag{A.4}$$

where $B(T,v)$ is the Planck function and $c1$ and $c2$ are the Planck constants. The total radiance that the AVHRR measures is computed by adding up the individual radiances that it receives in each small wavenumber region;

$$R(T) = \frac{\sum[B(T,\nu_n) * SRF(\nu_n]}{\sum SRF(\nu_n)} \tag{A.5}$$

where $\nu_n = \nu_1, \nu_2, \nu_3, ...\nu_N$ and $SRF(\nu_n)$ is the Spectral Response Function.

In practice, this is done by first setting T= 180K and do the calculation, then set T= 180.1 and repeat the calculation, then set T= 180.2, 180.3, ...339.8, 339.9, 340K and do the calculations. This results in a table of 1,600 blackbody temperatures and AVHRR radiances.

This large (temperature, radiance) table can be accurately replaced by only one Planck function, one equation. In this new Planck function, only the

temperature varies; the wavenumber is fixed at a central wavenumber ν_c. The temperature variable is also slightly changed, from blackbody temperature T to $T' = a + bT$, where a is usually about 0.2 - 0.5K, and b is approximately 0.998 or 0.999. Using only this one equation, one can duplicate the table to within an accuracy of about 0.001K.
The equation for the AVHRR radiance $R(T)$ becomes,

$$R(T) = \frac{c1\nu_c^3}{e^{(\frac{c2\nu_c}{T'})} - 1} \tag{A.6}$$

The constant $c1\nu_c^3$ has units of radiance, so call it R_0 and the constant $c2\nu_c$ has units of temperature, call it T_0. Now for the AVHRR, a very good analytic approximation that fits the AVHRR radiance R versus blackbody temperature T curve can be written as

$$R(T) = \frac{R_0}{e^{\frac{T_0}{T'}} - 1} \tag{A.7}$$

For simplicity let $T' = T$. The term $e^{\frac{T_0}{T}}$ is usually 100 or more, so neglect 1 compared to this term. Then,

$$R = \frac{R_0}{e^{\frac{T_0}{T}}} \tag{A.8}$$

or

$$e^{\frac{T_0}{T}} = \frac{R_0}{R} \tag{A.9}$$

and

$$\frac{T_0}{T} = log(\frac{R_0}{R}) \tag{A.10}$$

Taking differentials on both sides and rearranging,

$$dT = \frac{T^2 e^{(\frac{T_0}{T})} dR}{R_0 T_0} \tag{A.11}$$

The noise in the AVHRR radiance, dR, is about the same at $200K$ or $250K$ as it is at $300K$, so the ratio of temperature increments at two different temperatures is

$$\frac{dT}{dT_{300}} = (\frac{T}{300})^2 \frac{e^{\frac{T_0}{T}}}{e^{\frac{T_0}{300}}} \tag{A.12}$$

The specified NEdT at $300K$ is $0.12K$ for the AVHRR thermal channels, then call this dT_{300}. T_0 slightly differs for channel 4 and 5, For example, $T_0 = 1338.8K$ for NOAA-14, channel 4 and $1202.4K$ for channel 5. The actual δR values and NEdT limits for channels 4 and 5 of NOAA-14 for $190K$, $200K$, $200K$ and $250K$ are given below. The observed noise in the thermal channels is less and within NEdT limits.

Table A.1: Observed noise (δR) and NEdT limits for the thermal channels of the AVHRR/2 onboard NOAA-14

Brightness temperature (in K)	Channel 4		Channel 5	
	δR	NEdT limit	δR	NEdT limit
190	0.31	0.64	0.28	0.49
200	0.27	0.50	0.25	0.40
220	0.20	0.33	0.18	0.28
250	0.13	0.20	0.11	0.18

Appendix B

Cloud detection algorithm CLAVR-1

The cloud detection algorithm used in this study is known as CLAVR-1, which is an improved version after experience with the original CLAVR algorithm. CLAVR-1 is a hierarchical decision-tree based cloud detection algorithm which employs a series of tests that use the thresholds and exploit heterogeneity in clouds. It also makes use of spectral signatures of clouds in all five channels of AVHRR. Details about the algorithm, tests and their thresholds are given below.

Cloud tests:

A pixel array of size 2x2 is passed through the following tests. If all pixels fail the tests, then they are called clear. If they pass the tests, they are cloudy or partly cloudy.

- RGCT (Reflectance Gross Cloud Test): Channel 2 or channel 1 reflectance is compared to a threshold.
- RUT (Reflectance Uniformity Test): Difference between maximum and minimum channel 2 or 1 reflectance in the 2x2 array is compared to a threshold.

- RRCT (Reflectance Ratio Cloud Test): Ratio of channel 2 to channel 1 is compared to a threshold.

- C3AT/C3AR (Ch 3 Albedo Test/Restoral): Channel 3 albedo is compared to a threshold, whereby, Ch 3 albedo is computed as

$$C_3AT = \frac{\pi \delta R_3}{\cos(Z) E_s S_3} 100\% \tag{B.1}$$

with

$$\delta R_3 = B(T_3) - B(T_{3e}) \tag{B.2}$$

and

$$T_{3e} = \frac{b}{a} T_4 - \frac{c}{a} T_5 + \frac{d}{a} \tag{B.3}$$

where, E_s = Square of Earth-to-Sun distance ratio,
Z = Solar zenith angle, and
T_3, T_4 and T_5 are channel 3, 4 and 5 brightness temperatures, respectively. The coefficients S_3, a, b, c and d are given below.

Satellite	S_3	a	b	c	d
NOAA-7	16.0872	1.000000	-2.535500	1.56201	-6.71000
NOAA-9	16.1510	0.982490	-2.659000	1.68550	-1.25000
NOAA-11	16.0707	0.962422	-2.127582	1.16516	-0.74000
NOAA-14	15.8066	1.000000	-2.915924	1.92754	-1.21284

- TUT/TUR (Thermal Uniformity Test/Restoral): Channel 4 brightness temperatures are compared to a threshold.

- FMFT (Four Minus Five Test): (Channel 4 - channel 5) is compared with a threshold (T_{FMFT}), which is given by

$$T_{FMFT} = A_0 T_4 + A_1 T_4 + A_2 T_4 + A_3 T_4 + A_4 T_4 + A_5 T_4 \tag{B.4}$$

This equation for the ocean is applied when $240K < T_4 < 287K$. When $T_4 < 240K$, the threshold is set to zero. If $T_4 > 295K$, it is set to $4.0K$.

For $287K < T_4 < 295K$, the following linear relation is used:

$$T_{FMFT} = 0.154(T_4 - 287) + 2.77 \tag{B.5}$$

For land surfaces, the FMFT threshold equation is applied in the T_4 range from $260K$ to $305K$. If $T_4 < 260K$, the threshold is set to zero; and if $T_4 > 305K$, it is set to $7.8K$, a number resulting from the inclusion of desert observations from AVHRR. When land surface temperatures become so high during daytime that channels 4 and/or 5 approach saturation values (viz., at and above about $315K$), the FMFT is suspended. The equation coefficients are given as:

Coefficient	FMFT-Ocean	FMFT-Land
A_0	9.27066E+04	-1.34436E+04
A_1	-1.79203E+03	1.94945E+02
A_2	1.38305E+01	-1.05635E+00
A_3	-5.32679E-02	2.53361E-03
A_4	1.02374E-04	-2.26786E-06
A_5	-7.85333E-08	0.0

- TGCT/TGCR (Thermal Gross Cloud Test/Restoral): Ch 4 temperature in the array is compared to a threshold value.

- Cone of specular reflection (GAMMA): The restoral tests over ocean and Antarctica are applied when viewing within a specified angular distance from the specular reflection direction for a plane ocean surface. The half-angle of this cone, GAMMA, is defined as:

$$GAMMA = cos^{-1}(\cos(Z_o)\cos(Z) + \sin(Z_o)\sin(Z)cos(A)) \tag{B.6}$$

where Z_o and Z are solar and satellite zenith angles, respectively, and A is relative azimuth angle ($A < 90°$ - viewing toward the specular ray, $A > 90°$ - viewing away from it).

Table B.1: Thresholds for cloud tests for daytime CLAVR-1 algorithm

Tests	Land		Ocean	
Cloud/mixed tests	Channel used	Threshold	Channel used	Threshold
RGCT	1	$> 44\%$	2	$> 30\%$
RUT	1	$> 9\%$	2	$> 0.3\%$
RRCT	1, 2	$0.9 < R < 1.1$	1, 2	$0.9 < R < 1.1$
C3AT	3, 4, 5	$> 6\%$	3, 4, 5	$> 3\%$
TUT	4	$> 3K$	4	$> 0.5K$
FMFT	4, 5	$> T_{FMFT}$	4, 5	$> T_{FMFT}$
TGCT	4	$< 249K$	4	$< 271K$
Clear Restoral tests				
C3AR	3	$< 3\%$	3	$< 3\%$
TUR	4	$< 1K$	4	$< 0.5K$
TGCR	4	$> 293K$	NA	NA

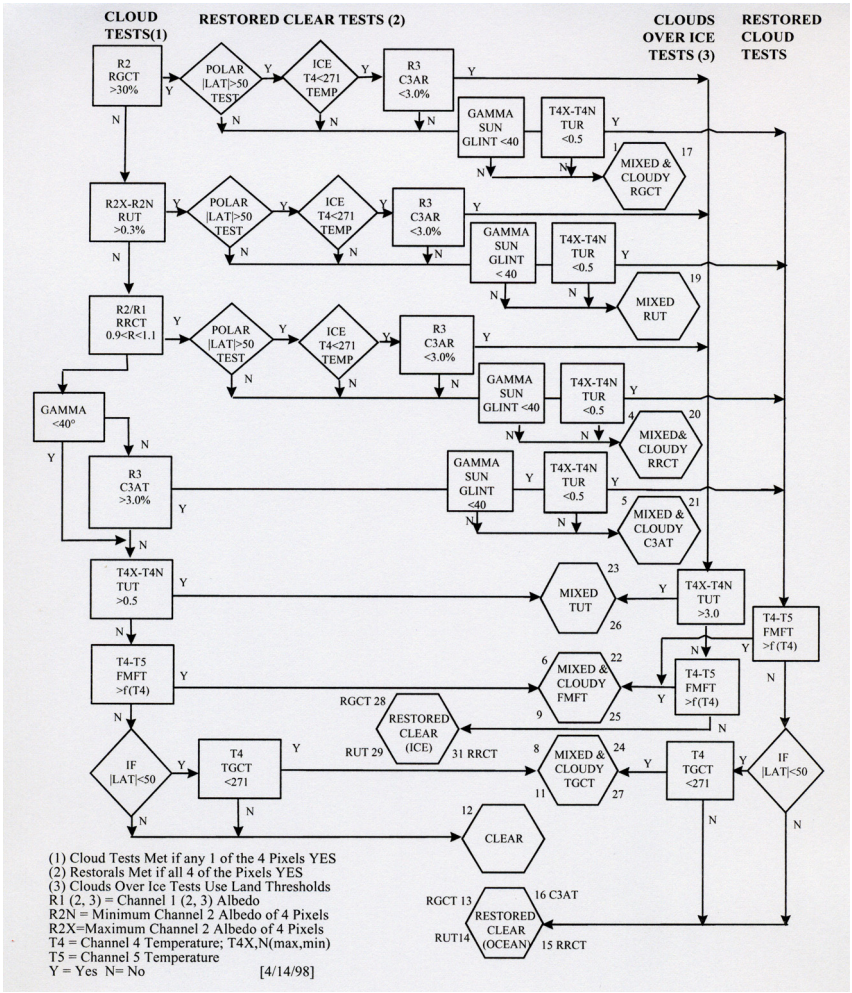

Figure B.1: CLAVR-1 daytime ocean algorithm

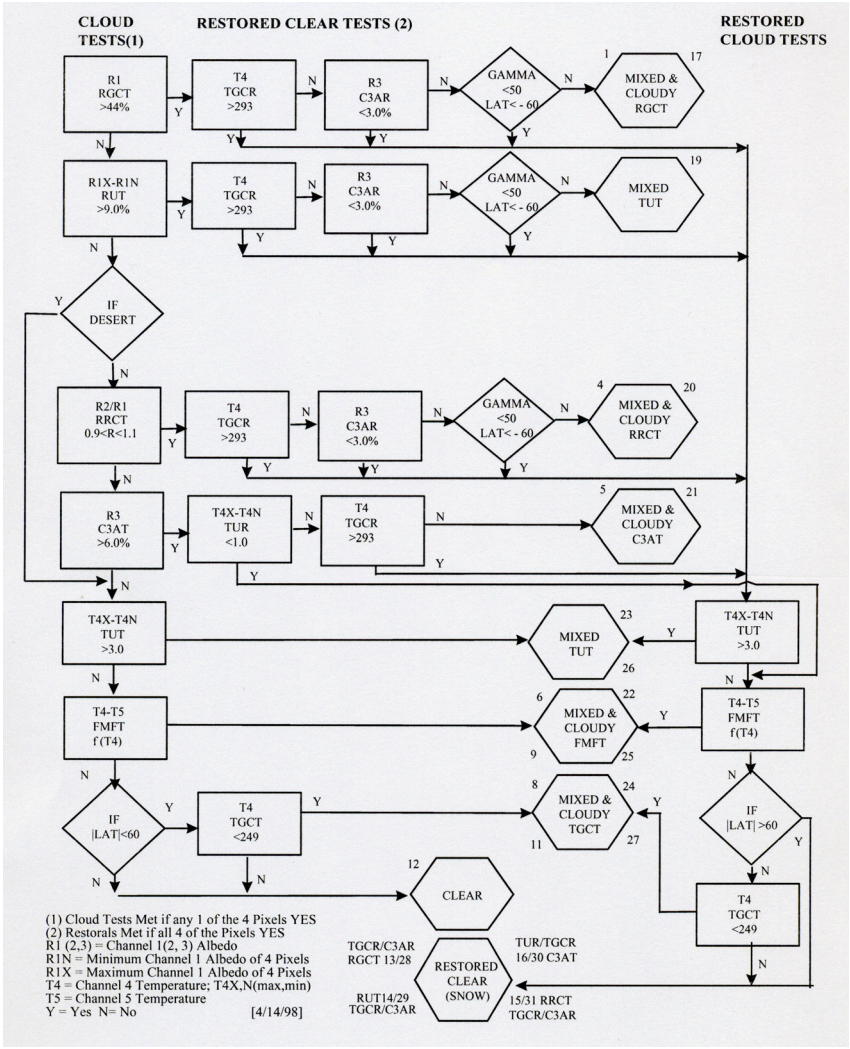

Figure B.2: CLAVR-1 daytime land algorithm

Bibliography

[1] Intergovernmantal Panel on Climate Change (IPCC), *Climate change: The Scientific Basis*, Contribution of Working Group I to the Thirst Assessment Report of the Intergovernmantal Panel on Climate Change, Editor J. T. Houghton et. al., Cambridge University Press, New York, 2001, pp. 881.

[2] V. Ramanathan, P. J. Crutzen, J. T. Kiehl and D. Rosenfeld, "Aerosols, climate and hydrological cycle," *Science*, vol. 294, pp. 2119-2124, 2001.

[3] Y. J. Kaufman, Didier Tanre, and Olivier Boucher, "A satellite view of aerosols in the earth system," *Nature*, vol. 419, pp. 215-223, 2002.

[4] M. O. Andreae, D. Rosenfeld, P. Artaxo, A. A. Costa, G. P. Frank, K. M. Longo, and M. A. F. Silvia-Dias, "Smoking rain clouds over the Amazon," *Science*, vol. 303, pp. 1337-1342, 2004.

[5] Francois Marie Breon, Didier Tanre, and Sylvia Generoso, "Aerosol effect on cloud droplet size monitored from satellite," *Science*, vol. 295, pp. 834-837, 2002.

[6] Y. J. Kaufman and Teruyuki Nakajima, "Effect of Amazon smoke on cloud microphysics and albedo," *J. App. Met.*, vol. 32, pp. 729-743, 1993.

[7] Andreas Keil, Manfred Wendisch, and Jost Heintzenberg, "A case study on microphysical and radiative properties and power-plant-originated clouds," *Atm. Res.*, vol. 63, pp. 291-301, 2002.

[8] Daniel Rosenfeld, Suppression of rain and snow by urban and industrial air pollution," *Science*, vol. 287, pp. 1793-1796, 2000.

[9] M. D. King, Y. J. Kaufman, W. P. Menzel, and Didier Tanre, "Remote sensing of cloud, aerosol and water vapour properties from Moderate Resolution Imaging Spectrometer (MODIS)," *IEEE Trans. Geosci. Remote Sensing*, vol. 30, no. 1, pp. 2-27, 1992.

[10] Arthur P. Cracknell, *Advanced Very High Resolution Radiometers (AVHRR)*, Taylor and Francis Books Ltd, April 1997, pp.968.

[11] K. B. Kidwell, *Polar orbiter data user's guide*, US Department of Commerce, NESDIS, NOAA, Washington, DC, USA, 1998.

[12] C. R. N. Rao, *Prelaunch calibration of channels 1 and 2 of the AVHRR*, NOAA Technical Report NESDIS 36, Department of Commerce, Washington, D.C., 1987.

[13] C. R. N. Rao and J. Chen, "Inter-satellite calibration linkages for the visible and near-infrared channels of the Advanced Verh High Resolution Radiometer on the NOAA-7, -9 and -11 spacecraft," *Int. J. Remote Sens.*, vol. 16, pp. 1931-1942, 1995.

[14] Y. J. Kaufman and B. N. Holben, "Calibration of AVHRR visible and near-IR bands by atmospheric scattering, ocean glint and desert reflection," *Int. J. Remote Sens.*, vol. 14, no.1, pp. 21-52, 1993.

[15] N. Che and J. C. Price, "Survey of radiometric calibration results and methods for visible and near infrared channels of NOAA-7, -9 and -11 1 AVHRRs," *Remote Sens. Environ.*, vol. 41, pp. 19-27, 1992.

[16] M. Jin and R. E. Treadon, "Correcting the orbit drift effect on AVHRR land surface skin temeprature measurements," *Int. J. Remote Sens.*, Vol. 24, No. 22, pp. 4543-4558, 2003.

[17] Alexander P. Trischenko, Gunar Fedosejevs, Zhanqing Li, and Josef Cihlar, "Trends and uncertainties in thermal calibration of AVHRR radiometers onboard NOAA-9 to NOAA-16," *J. Geophys. Res.*, vol. 107, no. D24, pp. 4778, 2002.

[18] M. E. James and S. N. V. Kalluri, "The pathfinder AVHRR land data set: An improved coarse resolution data set for terrestrial monitoring," *Int. J. Remote Sens.*, vol. 15, no. 17, pp. 3347-3363, 1994.

[19] Howard R. Gordon, James W. Brown, and Robert H. Evans, "Exact Rayleigh scattering calculations for use with the Nimbus-7 Coastal Zone Colour Scanner," *Applied Optics*, vol. 27, no. 5, pp. 862-871, 1988.

[20] L. L. Stowe, P. A. Davis, and E. P. McClain, "Scientific basis and initial evaluation of the CLAVR-1 global Clear/Cloud classification algorithm for Advanced Very High Resolution Radiometer," *J. Atm. Oceanic Tech.*, vol. 16, pp. 656-681, 1999.

[21] R. K. Kaufmann, Liming Zhou, Yuri Knyazikhin, Nikolay V. Shabanov, Ranga B. Myeneni, and C. J. Tucker, "Effect of orbital drift and sensor changes on the time series of AVHRR vegetation index data," *IEEE Trans. Geosci. Remote Sensing*, vol. 38, no. 6, pp. 2584-2597, 2000.

[22] M. L. Steyn-Ross, D. A. Steyn-Ross and A. Jelenk, "Comparison of atmospheric correction algorithms for deriving sea surface temeprature from AVHRR," *Int. J. Remote Sens.*, vol. 20, no. 18, pp. 3515-3531, 1999.

[23] G. G. Gutman, "On the monitoring of land surface temperatures with the NOAA/AVHRR: removing the effect of satellite orbit drift," *Int. J. Remote Sens.*, vol. 20, no. 17, pp. 3407-3413, 1999.

[24] J. L. Privette, C. Fowler, G. A. Wick, D. Baldwin and W. J. Emery, "Effects of orbital drift on Advanced Very High Resolution Radiometer products: Normalized Difference Vegetation Index and Sea Surface Temperature," *Remote Sens. Environ.*, vol. 53, pp. 164-171, 1995.

[25] J. Key and A.J. Schweiger, "Tools for atmospheric radiative transfer: Streamer and FluxNet," *Computers & Geosciences*, 24(5), 443-451, 1998.

[26] Olaf Krüger and Hartmut Grassl, "The indirect aerosol effect over Europe," *Geophys. Res. Lett.*, vol. 29, 2002.

[27] Olaf Krüger, Roman Marks, and Hartmut Grassl, "Influence of pollution on cloud reflectance," *J. Geophys. Res.*, vol. 109, 2004.

[28] EMEP Status Report with respect to Measurements, Modelling and Emissions of particulate matter in EMEP: An integrated approach, Joint CCC and MSC-W report, EMEP MSC-W Note 5/100, Norway, Aug. 2000.

[29] W. F. Cooke and J. J. N. Wilson, "A global black carbon aerosol model," *J. Geophys. Res.*, vol. 101 no. D14, pp. 19395-19409, 1996.

[30] C. Liousse, J. E. Penner, C. Chuang, J. J. Walton, H. Eddleman, and H. Cachier, "A global three-dimensional model study of carbonaceous aerosols," *J. Geophys. Res.*, vol. 101, no. D14, pp. 19411-19432, 1996.

[31] International Maritime Organization (IMO) study on greenhouse gas emissions from ships, MEPC, 45(8), 2000.

[32] J. J. Corbett, P. S. Fischbeck, and S. N. Pandis, "Global nitrogen and sulfur inventories for oceangoing ships," *J. Geophys. Res.*, vol. 104(3), pp. 3457-3470, 1999.

[33] J. J. Corbett, and H. W. Köhler, "Updated emissions from ocean shipping," *J. Geophys. Res.*, vol. 108, 2003.

[34] O. Endresen, E. Sørgård , J.K. Sundet, S.B. Dalsøren, I.S.A. Isaksen, T.F. Berglen, and G. Gravir, "Emission from international sea transportation and environmental impact," *J. Geophys. Res.*, vol. 108, pp. 4560, 2003.

[35] V. Eyring, H. W. Köhler, J. van Aardenne, and A. Lauer, "Emissions from international shipping. Part 1: The last 50 years," *J. Geophys. Res.*, accepted, 2005.

[36] Final report from Entec UK Ltd for the European Commission, *Quantification of emissions from ships associated with ship movements between ports in the European Community*, can be found at
http://europa.eu.int/comm/environment/air/background.htm#transport

[37] S. Beirle, U. Platt, R. von Glasow, M. Wenig, and T. Wagner, "Estimate of nitrogen oxide emissions from shipping by satellite remote sensing," *Geophys. Res. Lett.*, vol. 31, L18102, doi:10.1029/2004GL020312, 2004.

[38] H. Bovensmann, J. P. Burrows, M. Buchwitz, J. Frerick, S. Noël, V. V. Rozanov, K. V. Chance, and A. H. P. Goede, "SCIAMACHY - Mission objectives and measurement modes," *J. Atmos. Sci.*, vol. 56 (2), pp. 127-150, 1999.

[39] J. P. Burrows, M. Weber, M. Buchwitz, V. Rozanov, A. Ladstätter-Weißenmeyer, A. Richter, R. DeBeek, R. Hoogen, K. Bramstedt, K.-U. Eichmann, and M. Eisinger, "The Global Ozone Monitoring Experiment (GOME): Mission Concept and First Scientific Results," *J. Atm. Sci.*, vol. 56, pp. 151-175, 1999.

[40] Peter v. Hobbs, Timothy J. Garrett, Ronald, J. Ferek, Scott R. Strader, Dean A. Hegg, Glendon M. Frick, William A. Hoppel, Richard F. Gasparovic, Lynn M. Russell, Douglas W. Johnson, Colin O´Dowd, Philip A. Durkee, Kurt E. Nielson, and George Innis, "Emissions from ships with respect to their effects on clouds," *J. Atm Sci.*, vol. 57, pp. 2570-2590, 2000.

[41] James G. Hudson, Timothy J. Garrett, Peter V. Hobbs, Scott R. Strader, Yonghong Xie, and Seong Soo Yum, "Cloud condensation nuclei and ship tracks," *J. Atm Sci.*, vol. 57, pp. 2696-2706, 2000.

[42] B. N. Holben, D. Tanre, A. Smirnov, T. F. Eck, I. Slutsker, N. Abuhassan, W. W. Newcomb, J. Schafer, B. Chatenet, F. Lavenue, Y. J. Kaufman, J. Vande Castle, A. Setzer, B. Markham, D. Clark, R. Frouin, R. Halthore, A. Karnieli, N. T. O'Neill, C. Pietras, R. T.Pinker, K. Voss, and G. Zibordi, "An emerging ground-based aerosol climatology: Aerosol Optical Depth from AERONET," *J. Geophys. Res.*, vol. 106, pp. 12067-12097, 2001.

[43] V. Vestreng et al, Inventory review 2004. Emission data reported to CLRTAP and the NEC Directive, *EMEP/EEA Joint Review report*, EMEP/MSC-W Note 1, July 2004.

[44] Abhay Devasthale, Olaf Krüger and Hartmut Grassl, "Change in cloud top temperatures over Europe," *IEEE Geosci. Remote Sensing Lett.*, vol. 2, no.3, pp. 333-336, 2005.

[45] Abhay Devasthale, Olaf Krüger and Hartmut Grassl, "Impact of ship emissions on cloud properties over coastal areas," in preparation, 2005.

Acknowledgements

I am highly obliged to both of my advisors, Dr. Olaf Krüger and Prof. Hartmut Graßl, for their timely and valuable guidence. Prof. Graßl showed keen interest in the subject and spared his valuable time as and when required. Special thanks to the University of Hamburg (Fachbereich Geowissenschaften), IMPRS-ESM and DFG/SFB512 for the funding and support during this work. Thanks to the IMPRS-ESM and MPI for Meteorology for providing computing, educational and bureaucratic resources and help. I am also very thankful to all people who directly or indirectly helped me during this work. The availability of free AVHRR GAC level 1b data from the Satellite Active Archive (NOAA/NESDIS), AERONET data, and EMEP emission data is acknowledged.

MPI-Examensarbeit-Referenz:
Examensarbeit Nr. 1-82 bei Bedarf bitte anfragen:
MPI für Meteorologie, Abtlg.: PR, Bundesstr. 53, 20146 Hamburg

MPI-Report-Referenz:
MPI-Report Nr. 1-351 bei Bedarf bitte anfragen:
MPI für Meteorologie, Abtlg.: PR, Bundesstr. 53, 20146 Hamburg

---

Beginn einer neuen Veröffentlichungsreihe des MPIM, welche die vorherigen Reihen "Reports" und "Examensarbeiten" weiterführt:

„Berichte zur Erdsystemforschung" , „*Reports on Earth System Science*", ISSN 1614-1199
Sie enthält wissenschaftliche und technische Beiträge, inklusive Dissertationen.

Berichte zur Erdsystemforschung Nr.1 Juli 2004	**Simulation of Low-Frequency Climate Variability in the North Atlantic Ocean and the Arctic** Helmuth Haak
Berichte zur Erdsystemforschung Nr.2 Juli 2004	**Satellitenfernerkundung des Emissionsvermögens von Landoberflächen im Mikrowellenbereich** Claudia Wunram
Berichte zur Erdsystemforschung Nr.3 Juli 2004	**A Multi-Actor Dynamic Integrated Assessment Model (MADIAM)** Michael Weber
Berichte zur Erdsystemforschung Nr.4 November 2004	**The Impact of International Greenhouse Gas Emissions Reduction on Indonesia** Armi Susandi
Berichte zur Erdsystemforschung Nr.5 Januar 2005	**Proceedings of the first HyCARE meeting, Hamburg, 16-17 December 2004** Edited by Martin G. Schultz
Berichte zur Erdsystemforschung Nr.6 Januar 2005	**Mechanisms and Predictability of North Atlantic - European Climate** Holger Pohlmann
Berichte zur Erdsystemforschung Nr.7 November 2004	**Interannual and Decadal Variability in the Air-Sea Exchange of CO2 - a Model Study** Patrick Wetzel
Berichte zur Erdsystemforschung Nr.8 Dezember 2004	**Interannual Climate Variability in the Tropical Indian Ocean: A Study with a Hierarchy of Coupled General Circulation Models** Astrid Baquero Bernal
Berichte zur Erdsystemforschung Nr9 Februar 2005	**Towards the Assessment of the Aerosol Radiative Effects, A Global Modelling Approach** Philip Stier
Berichte zur Erdsystemforschung Nr.10 März 2005	**Validation of the hydrological cycle of ERA40** Stefan Hagemann, Klaus Arpe and Lennart Bengtsson
Berichte zur Erdsystemforschung Nr.11 Februar 2005	**Tropical Pacific/Atlantic Climate Variability and the Subtropical-Tropical Cells** Katja Lohmann

MPI-Examensarbeit-Referenz:
Examensarbeit Nr. 1-82 bei Bedarf bitte anfragen:
MPI für Meteorologie, Abtlg.: PR, Bundesstr. 53, 20146 Hamburg

MPI-Report-Referenz:
MPI-Report Nr. 1-351 bei Bedarf bitte anfragen:
MPI für Meteorologie, Abtlg.: PR, Bundesstr. 53, 20146 Hamburg

Berichte zur Erdsystemforschung Nr.12 Juli 2005	**Sea Ice Export through Fram Strait: Variability and Interactions with Climate**- Torben Königk
Berichte zur Erdsystemforschung Nr.13 August 2005	**Global oceanic heat and fresh water forcing datasets based on ERA-40 and ERA-15** Frank Röske
Berichte zur Erdsystemforschung Nr.14 August 2005	**The** HAM**burg** O**cean** C**arbon** C**ycle Model HAMOCC5.1 - Technical Description Release 1.1** Ernst Maier-Reimer, Iris Kriest, Joachim Segschneider, Patrick Wetzel
Berichte zur Erdsystemforschung Nr.15 Juli 2005	**Long-range Atmospheric Transport and Total Environmental Fate of Persistent Organic Pollutants - A Study using a General Circulation Model** Semeena Valiyaveetil Shamsudheen


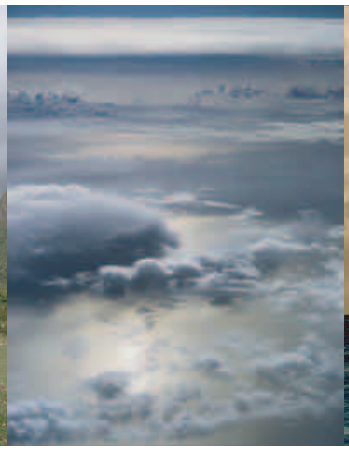


ISSN 1614-1199